

## REVISION 1

1

### 2 **Hydrogen diffusion in Ti-doped forsterite and the preservation of** 3 **metastable point defects**

4 Michael C. Jollands<sup>1,2\*</sup>, José Alberto Padrón-Navarta<sup>3</sup>, Jörg Hermann<sup>1,4\*</sup>, Hugh St.C.  
5 O'Neill<sup>1</sup>

6 <sup>1</sup>Research School of Earth Sciences, Australian National University, Canberra, ACT 0200, Australia

7 <sup>2</sup>Institut des Sciences de la Terre, Bâtiment Géopolis, Université de Lausanne, 1015 Lausanne,  
8 Switzerland

9 <sup>3</sup>Géosciences Montpellier, CNRS & Univ. Montpellier, 34095 Montpellier, France

10 <sup>4</sup>Institute of Geological Sciences, University of Bern, 3012 Bern, Switzerland

11 \*present address

12 Correspondence: [michael.jollands@unil.ch](mailto:michael.jollands@unil.ch)

13

14 **Keywords:** Diffusion; Point defects; Nominally Anhydrous Minerals; FTIR  
15 spectroscopy

16

#### 17 **Abstract**

18 The effect of trace concentrations of Ti on the rate and mechanism of hydrogen  
19 diffusion in pure forsterite was investigated experimentally. Forsterite doped with  
20 350-400 ppm Ti (predominantly octahedral Ti<sup>3+</sup>, minor tetrahedral Ti<sup>4+</sup>) was prepared  
21 by diffusing Ti into pure synthetic forsterite at high temperature (1500 °C), very low  
22 oxygen fugacity (~QFM-5) at atmospheric pressure. The Ti-doped forsterite was then  
23 diffusively hydroxylated in a piston-cylinder apparatus at much lower temperatures  
24 (650-1000 °C) and higher oxygen fugacities, at 1.5-2.5 GPa, with chemical activities  
25 buffered by forsterite-enstatite or forsterite-periclase and partial pressure of H<sub>2</sub>O equal  
26 to total pressure. This produced hydrogen concentration-distance profiles of several

27 hundred micrometres in length. Diffusion of hydrogen through the Ti-doped forsterite,  
28 even at very high  $fO_2$ , does not lead to redox re-equilibration of the high  $Ti^{3+}/\Sigma Ti$  ratio  
29 set during the synthesis of the starting material at extremely reducing conditions – the  
30 metastable point defects are partially preserved.

31 Three main hydroxylated point defects are observed – hydroxyl is associated with  $Ti^{4+}$   
32 (titano-clinohumite point defects),  $Ti^{3+}$  (and possibly other trivalent cations) and M-  
33 site vacancies. Concentration-distance profiles represent an interplay between  
34 diffusion and reaction (i.e. site rearrangement) to form the observed point defects. In  
35 all experiments, the concentration-distance profiles of the hydroxylated Ti defects  
36 coincide with the concentration-distance profiles of the M-site vacancy substitution,  
37 with the same crystallographic anisotropy. This suggests that the macroscopic  
38 movement of hydrogen through the crystal is due to one diffusion mechanism (the  
39 diffusion of hydroxylated M-site vacancies). The net H diffusion coefficient  
40 ( $\log D(\Sigma H)$ ), between 650-1000 °C, is:

41

$$42 \quad \log D(\Sigma H) = \log D_0(\Sigma H) + \left( \frac{-223(\pm 8) \text{ kJmol}^{-1}}{2.3RT} \right)$$

43

44 Where the value of  $\log D_0(\Sigma H)$  parallel to [100] and [001] directions are  $-3.0 \pm 0.4$  and  
45  $-2.2 \pm 0.4$  respectively; diffusion is therefore around one order of magnitude faster  
46 along the  $c$  axis than along the  $a$  axis. The diffusion of hydrogen is slightly faster in  
47 Ti-doped forsterite than in pure forsterite. There is no effect of chemical activity or  
48 oxygen fugacity on the rate of diffusion. Hydrogen diffusion profiles represent a  
49 complex interplay between the movement of H through the crystal lattice and point-  
50 defect reactions to maintain charge balance.

51

52

53

### **Introduction**

54 Since the discovery of hydroxyl (OH) stretching bands in olivine nearly half a century  
55 ago (Beran, 1969), considerable effort has been expended in determining the  
56 concentration and speciation of hydrogen in nominally anhydrous mantle phases.

57 Understanding this is a prerequisite for understanding the total water budget of the  
58 Earth (e.g. Bell and Rossman, 1992; Bolfan-Casanova, 2005; Demouchy and Bolfan-  
59 Casanova, 2016 Hirschmann et al., 2005; Smyth et al., 2006). Several studies have  
60 attempted to quantify the amount of water in mantle olivine by measuring its  
61 concentration in rapidly emplaced xenoliths and xenocrysts where the original mantle  
62 water signature should be preserved (e.g. Bell et al., 2004; Grant et al., 2007;

63 Kitamura et al., 1987). However, the extent to which mantle olivine can maintain its  
64 original water signature between being entrained in melt to being erupted/emplaced,  
65 for example, is a function of the hydrogen diffusion mechanism and its rate, which is  
66 still a matter of debate (e.g. Demouchy and Mackwell, 2003; 2006; Du Frane and  
67 Tyburczy, 2012; Ferriss et al., 2015; Kohlstedt and Mackwell, 1998; Mackwell and  
68 Kohlstedt, 1990; Padrón-Navarta et al., 2014, Thoraval and Demouchy, 2014).

69 Additionally, if the diffusion rate of hydrogen is known, and diffusive water loss is  
70 observed in olivine xenocrysts, constraints can be placed on the duration of ascent and  
71 emplacement (e.g. Demouchy et al., 2006; Denis et al., 2013; Peslier and Luhr, 2006;  
72 Peslier et al., 2008, 2015; Peslier and Bizimis, 2015). The water content of olivine can  
73 also be an indicator of the petrogenetic processes accompanying the entrainment of  
74 their host xenoliths by ascending melts from the mantle (e.g. Tollan et al., 2015).

75 At least four main mechanisms of hydroxyl substitution in olivine have been  
76 observed: OH may be associated with Si vacancies, M-site vacancies (vacancies in the  
77 octahedral site), traces of trivalent cations, or with  $Ti^{4+}$  in a point defect resembling a  
78 unit of the titano-clinohumite structure. The coupled hydrogen-titanium substitution  
79 studied here may also be an important mechanism for transport of water into the upper  
80 mantle (Hermann et al., 2007; Shen et al., 2014; Wirth et al., 2001) and storage of  
81 water in olivine therein (Berry et al., 2005, 2007b; Walker et al., 2007).

82 The diffusion of hydrogen is likely to be even more complex; several different  
83 diffusion mechanisms have been identified, each with different diffusion rates  
84 (Demouchy and Mackwell, 2003, 2006; Du Frane et al, 2012; Ingrin and Blanchard,  
85 2006; Kohlstedt and Mackwell, 1998; Mackwell and Kohlstedt, 1990; Padrón-Navarta  
86 et al, 2014). In addition, the different point defects may interact with one another  
87 inside the crystal (e.g. Padrón-Navarta et al, 2014), thus creating or annihilating  
88 hydroxylated sites. Understanding these issues is necessary both for interpreting  
89 hydrogen in natural olivine and designing future experiments.

90 In this study, we aim to determine if trace quantities (hundreds of parts per million) of  
91 titanium affect the rate of H diffusion relative to pure forsterite. For this purpose, we  
92 have prepared forsterite crystals with a given amount of Ti, and a point-defect  
93 structure that is relatively well constrained and homogeneous based on the findings  
94 from an extensive study of Ti diffusion in forsterite in anhydrous conditions (Jollands  
95 et al., submitted).

96

97

## Methods

98

### 99 Preparation and characterization of starting material

100  
101 Pure synthetic forsterite (grown by the Czochralski method, as used by Jollands et al.,  
102 2014; purity reported in Zhukova et al., 2014) was doped with 350-400 ppm Ti by  
103 diffusing this element into the crystal until a near constant concentration was reached  
104 throughout. Oriented slabs of approximately 1x3x12 mm were cut from a single  
105 crystal of pure forsterite with the shortest axis corresponding to *c*, i.e. the largest face  
106 of the slab was parallel to (001). This orientation was chosen because Ti diffuses  
107 fastest along [001] (Spandler and O'Neill 2010; Jollands et al., submitted). A pre-  
108 sintered powder of forsterite-karooite-geikielite ( $\text{Mg}_2\text{SiO}_4\text{-MgTi}_2\text{O}_5\text{-MgTiO}_3$ ) was  
109 mixed with polyethylene oxide glue and pasted onto the two (001) faces; this three-  
110 phase mix was chosen as it gave the fastest Ti diffusion at 1500 °C without any partial  
111 melting (Jollands et al., submitted). The crystal-powder couple was then annealed in a  
112 gas mixing furnace at very low  $f\text{O}_2$  (QFM -5.2; 97% CO - 3% CO<sub>2</sub>) for ~6 weeks at  
113 1500 °C to allow the Ti to homogenise through the crystal by diffusion on octahedral  
114 sites. The powder partially sintered to the slab surface; this was removed by gentle  
115 polishing. This also likely removed any areas of high Ti associated with Ti diffusion  
116 on tetrahedral sites. The doping gave the crystal a slight bluish hue. The slab was then  
117 cut into cubes of approximately 1x1x1 mm, with sides parallel to the slab edges such  
118 that each cube was oriented with faces representing (001), (010) and (100).  
119 One such cube was mounted in epoxy, ground down by around 300 µm to reveal the  
120 crystal core, and analysed from rim to rim (whole crystal traverse) by laser ablation  
121 ICP-MS using a slit-shaped 6x100 µm beam from a 193 nm Lambda Physik Complex  
122 excimer laser coupled to an Agilent 7700 ICP-MS (as described in Jollands et al.  
123 2014). In each time slice, <sup>47</sup>Ti was counted for 0.3 s, <sup>57</sup>Fe and <sup>27</sup>Al (likely  
124 contaminants) for 0.05 s and <sup>29</sup>Si (internal standard) for 0.01 s. The pulse rate was 5

125 Hz, energy was maintained around 50 mJ (monitored by an internal energy meter via  
126 a beam splitter at the point of exit from the laser source), NIST610 was used as  
127 primary standard and data were processed using Iolite (Paton et al., 2011) against the  
128 standard values of Jochum et al. (2011) ( $452 \pm 10$  ppm Ti) with no glass-olivine matrix  
129 correction made.

130 Full homogenization (along [001]) had not occurred (Figure 1); the core (~350 ppm)  
131 was slightly lower in Ti than the rim (400 ppm). In addition, the Al concentration  
132 profile showed some heterogeneity; one side of the crystal had approximately double  
133 the Al concentration than the other. The Al profile is comprised of two flat sections;  
134 one side of the crystal has  $7.7 \pm 1.1$  ppm and the other  $13.9 \pm 2.3$  ppm. The reason for  
135 this behaviour is unknown; it may be that the Czochralski growth method led to some  
136 minor sector zoning in the original crystal. The small amount of Fe (10-50 ppm) is  
137 likely from contamination in the gas-mixing furnace; this is expected to be all  $\text{Fe}^{2+}$  at  
138 the very reducing conditions of the Ti doping step (Mallmann and O'Neill, 2010).  
139 Early preliminary attempts to homogenize cubes (i.e. cut 1x1x1 mm cubes *before the*  
140 *anneal*, immerse these in powder then anneal) were unsuccessful, the cubes were  
141 generally cracked after the high T low  $f\text{O}_2$  anneal, which precluded their use in  
142 hydroxylation experiments.

143

#### 144 **Diffusion experiments**

145

146 Previous experiments to determine the diffusion of hydrogen in minerals have been  
147 hampered by the difficulty of recovering whole, uncracked crystals from the piston  
148 cylinder or cold-seal vessels after diffusion anneals (e.g. Demouchy and Mackwell,  
149 2003, 2006). The method used in this study, once refined, had a 100% success rate of

150 crystal recovery of a total of 8 experiments. Large (6.3 mm outer diameter) thick-  
151 walled, cold-swage silver capsules were used; the capsule and snug-fitting lid were  
152 precision-milled from a solid bar of high-purity silver (Figure 2). The capsule design  
153 and specifications are presented in Hack and Mavrogenes (2006). Cubes of forsterite  
154 were placed inside the capsules in a buffer of either forsterite+enstatite or  
155 forsterite+periclase (sintered from reagent grade MgO and SiO<sub>2</sub> powders, pressed into  
156 pellets, fired at 1400 °C in air and then reground). Where *f*O<sub>2</sub> buffers were used (e.g.  
157 Re-ReO<sub>2</sub> or Ag-Ag<sub>2</sub>O), these were packed into the capsule before the silica activity  
158 buffer. For reference, Re-ReO<sub>2</sub> and Ag-Ag<sub>2</sub>O are approximately NNO+2 and  
159 NNO+14, respectively at 850 °C, 1.5 GPa (see Pownceby and O'Neill, 1994; Assal et  
160 al 1997).

161 The capsules were filled to around 80-90% of their inside volume with the powder-  
162 crystal mix, then distilled water was added using a syringe until free water was visible  
163 on the top of the powder. Where too much water was added, the excess was removed  
164 using the corner of a tissue. The remainder of the capsule was then filled with the  
165 two-phase buffer powder. A lid was then placed inside the capsule, and pressed shut  
166 using a custom swaging tool. Excess Ag (the capsule is slightly deformed through  
167 swaging) was removed from the side of the capsule using a lathe to return it to a good  
168 cylindrical shape.

169 The amount of water added was very approximately calculated to fill the capsule  
170 (minus the volume of the crystal and powder) at peak anneal conditions using P-V-T  
171 values from Zhang and Duan (2005). In order to recover a crystal without cracks from  
172 shearing or torsion in the piston cylinder, it is important that the capsule should not  
173 deform excessively at any stage of the P-T path of the run. The large excess of water  
174 keeps the three-phase buffer material as a fairly loosely bound powder, which helps

175 removing the crystal from the capsule after the run without the necessity for any  
176 mechanical abrasion. The use of large silver capsules allows some flexibility; slightly  
177 too much water can be added without leakage, the excess being taken up by the  
178 capsule swelling into a barrel shape rather than losing their water (Figure 2). This  
179 represents a considerable improvement on previous designs using welded gold  
180 capsules; the capacity of the silver to stop leakage or H diffusion-out is significantly  
181 better (the walls are thicker), and, because no welding is necessary, more water can be  
182 added.

183 The capsules were run in an end-loaded 5/8" (15.9 mm) Boyd-type piston-cylinder  
184 apparatus using MgO-graphite-NaCl assemblies wrapped in low-friction Teflon foil.  
185 About 0.2 GPa pressure was applied initially at room temperature, before  
186 temperatures were ramped up at 100 °C/min, monitored continuously using a type B  
187 thermocouple sheathed in mullite, with the bead placed in intimate contact with the  
188 capsule by fitting into a pit drilled into the capsule lid. The pressure was increased  
189 concordantly with the temperature, in order to approximately follow the water  
190 isochore. The high thermal conductivity of silver coupled with the presence of a fluid  
191 phase keep thermal gradients extremely low (5-10 °C at 850°C) along the length of  
192 the capsule (Hack and Mavrogenes, 2006), despite being considerably longer (~12  
193 mm) than average capsules used in high temperature experiments.

194 Runs were stopped by turning off the power, such that the temperature dropped to  
195 <100 °C in around ten seconds, and the pressure was then slowly released, manually.  
196 Following decompression at the end of the run, the capsules were retrieved and  
197 pierced using a 1 mm drill bit to verify the presence of water. The top and bottom of  
198 the capsule was removed using a lathe, and the open cylinder was then placed into an  
199 ultrasonic bath to loosen the powder. Generally the buffer powder and crystal simply

200 fell out, but where it did not the powder was picked out using tweezers. The cube was  
201 further cleaned ultrasonically, oriented using the characteristic Si-O overtones in its  
202 FTIR spectrum, placed on a sticky tape on the (010) face, mounted in epoxy, and  
203 polished on two sides to around 400-600  $\mu\text{m}$  thickness (see Table 2 for thicknesses)  
204 using a diamond-impregnated grinding wheel, followed by diamond paste on cloth  
205 laps. No attempt was made to remove crystals from the epoxy after polishing.

206

### 207 **FTIR analysis**

208

209 With the exception of measurements to determine the polarisation of each point defect  
210 (see below), all other analyses were conducted using unpolarised light.

211 The mounts holding the doubly polished crystals were placed onto an automated  
212 mapping stage on a Bruker Hyperion IR microscope with a liquid nitrogen-cooled  
213 MCT detector coupled to a Bruker Tensor IR spectrometer. The measurement  
214 chamber was continuously purged with dry air. Measurements were generally  
215 composed of 128 scans with an effective spectral resolution of  $2\text{ cm}^{-1}$ .

216 Two different analytical routines were used. In 'profile' mode, the aperture was  
217 closed into a  $\sim 25 \times 200\ \mu\text{m}$  slit and unpolarised analyses were taken every  $5\ \mu\text{m}$  along  
218 a line from one side of the crystal to the other. This was advantageous in terms of the  
219 high spatial resolution (although the true spatial resolution is a complex function of  
220 the focal plane and analytical geometry and certainly poorer than  $25\ \mu\text{m}$ ) and  
221 favourable signal to noise ratio, but made the implicit assumption that diffusion was  
222 effectively one-dimensional along the length of the slit. This assumption might not be  
223 satisfied in such experiments where the diffusant (hydrogen) moves into the crystal  
224 from all sides, which would give diffusion profiles differing in shape from theoretical

225 expectations, and perhaps not reaching zero concentration in the middle of the crystal  
226 due to interference from diffusion from the other sides.

227 Accordingly, some crystals were also examined in two dimensions with unpolarised  
228 light, with a 50x50  $\mu\text{m}$  square aperture that mapped the entire crystal with 25-30  $\mu\text{m}$   
229 steps, such that all analyses were overlapping. Sub-samples of the map were then  
230 extracted along lines where diffusion appeared one-dimensional; i.e. no interference  
231 from the other sides. This method has poorer spatial resolution but gives greater  
232 confidence that the profiles are one-dimensional. Asymmetrical diffusion profiles  
233 (discussed later) could only be analysed using the profile mode; the spatial resolution  
234 of the mapping mode was too poor to resolve the short diffusion profiles associated  
235 with the asymmetry.

236 Spectra were corrected for atmospheric  $\text{H}_2\text{O}$  and  $\text{CO}_2$  using Bruker OPUS software,  
237 and the background subtracted using a concave rubberband correction with 64  
238 baseline points and three iterations. Given that polishing induced some minor  
239 topography in the sample (thicker in the centre, thinner at the edges), the spectra were  
240 then normalized to 1 cm thick using the empirical relationship of Shen et al. (2014)  
241 derived from the integrated area underneath the Si-O stretching band region (for  
242 measurements using unpolarised light). The integrated area ( $A_{\text{int}}$ ) of these overtones  
243 between 1625-2150  $\text{cm}^{-1}$  is related to thickness ( $T_{\text{sample}}$ ) using  $T_{\text{sample}} (\mu\text{m}) =$   
244  $A_{\text{int}}/0.553$ . Systematic biases may occur from this thickness correction, as the method  
245 was developed using randomly oriented grains, but for relative changes in OH content  
246 (i.e. diffusion profiles) this will have no effect. Analyses with epoxy contamination  
247 (at the crystal edge) were removed; these were identified both by the failure of the  
248 concave rubberband to fully remove background in the OH region (3100-3600  $\text{cm}^{-1}$ )  
249 as well as the characteristic overtones of organic material. Such spectra were removed

250 from consideration. The ‘interface’ spectra therefore represent the average spectra in  
251 the first 25  $\mu\text{m}$  when analyzing in profile mode, or the first 50  $\mu\text{m}$  in mapping mode  
252 (the assumption is made that the midpoint of the first analysis is at 12.5  $\mu\text{m}$  from the  
253 edge in profiles and 25  $\mu\text{m}$  in maps).

254

## 255 **Results**

256

### 257 **Infrared spectra**

258

259 Several unpolarised interface spectra were fitted to a series of ideal peaks (Figure 3),  
260 assumed as Gaussian, using the freeware OpticalFit, developed by, and available  
261 from, CSIRO Australia (MacRae and Wilson, 2008). All fitted peaks are considered  
262 to correspond to real absorption peaks in the spectra, with the exception of the low,  
263 broad peak at  $3252\text{ cm}^{-1}$ ; this is added to compensate for inadequate baseline  
264 subtraction in this region. The most prominent peak in interface spectra is always at  
265  $3351\text{ cm}^{-1}$ , with a shoulder formed by a peak at  $3349\text{ cm}^{-1}$  and an associated low peak  
266 at  $3313\text{ cm}^{-1}$ . These peaks are attributed to OH groups associated with  $\text{Ti}^{3+}$  on the M  
267 sites. The most likely substitution mechanism for this defect is a  $\text{Ti}^{3+}\text{-H}^+$  pair  
268 replacing two  $\text{Mg}^{2+}$  on the octahedral sites (e.g. Berry et al., 2007a), with  
269 stoichiometry  $(\text{Ti}^{3+}\text{H})\text{SiO}_4$ . This defect is notated [Ti-triv], where [triv] indicates a  
270 trivalent cation. The peaks were speculatively examined by Berry et al (2007a), who  
271 determined that a single trivalent cation-hydrogen pair can give up to three hydroxyl  
272 bands where the trivalent cation substitutes on both the M1 and M2 sites, due to the  
273 geometry of shared edges between octahedra.

274 The possibility for an  $\text{Al}^{3+}\text{-H}^+$  defect (i.e. [Al-triv]) is present ( $\sim 10$  ppm Al in the  
275 crystal), but there is no indication of this in the spectra ( $\text{Al}^{3+}$ -associated OH has a  
276 band at  $3345\text{ cm}^{-1}$  (Berry et al., 2007a).  
277 It is possible that an  $\text{Fe}^{3+}$ -associated OH defect is present (i.e. [Fe-triv]; peaks at 3350,  
278  $3331$  and  $3310\text{ cm}^{-1}$  according to Berry et al., 2007a) and responsible for the shoulder  
279 peak at  $3349\text{ cm}^{-1}$ . This is, however, unlikely, firstly because the Fe content in the  
280 crystal is low ( $\sim 10\text{-}50$  ppm in the majority of the crystal, up to 90 ppm in some parts)  
281 and secondly because the very low  $f\text{O}_2$  of the pre-anneal would favour nearly pure  
282  $\text{Fe}^{2+}$  and there is no apparent difference in spectra between crystals hydroxylated at  
283 high and low  $f\text{O}_2$ .  
284 The two prominent peaks at high wavenumbers ( $3571$  and  $3524\text{ cm}^{-1}$ ) are attributed to  
285 the Ti-clinohumite point defect ( $\text{MgTi}^{4+}\text{H}_2\text{O}_4$ ), herein [TiCh-PD], where a  $\text{Ti}^{4+}$  ion  
286 replaces a single  $\text{Mg}^{2+}$ , and charge balance is accomplished by replacement of  $\text{Si}^{4+}$   
287 with two  $\text{H}^+$  (Balan et al., 2011; Berry et al., 2005; Walker et al., 2007).  
288 The low, broad peak at  $3164\text{ cm}^{-1}$  is attributed to fully hydroxylated M-site vacancies;  
289 a single  $\text{Mg}^{2+}$  cation replaced by two  $\text{H}^+$  often observed in similar studies (Balan et  
290 al., 2011; Crepisson et al., 2014; Demouchy and Mackwell, 2003, 2006, Umemoto et  
291 al., 2011). This defect will be notated [Mg].  
292 After defining the three hydroxylated defect populations ([TiCh-PD], [Ti-triv], [Mg]),  
293 the integrated areas underneath each set of peaks were directly determined by  
294 measurement from the unpolarised baseline corrected spectra.  
295 The contributions from small, unidentified peaks at  $3428$ ,  $3580$  and  $3553\text{ cm}^{-1}$  are not  
296 considered in analysis of profiles.

297

## 298 **Determining water content**

299

300 In order to determine total integrated absorbance (i.e. the sum of polarised absorbance  
301 along the three orthogonal principal directions of the indicatrix), the polarization of  
302 each hydrous defect was determined by rotating the forsterite cube through 180° on  
303 two orthogonal sections below a stationary E-W polarizer and taking a series of  
304 infrared spectra. The start and end of the series for the section parallel to (010)  
305 corresponded to the electric vector parallel to [100] (E//[100]), and with E//[001]  
306 when the crystal was rotated 90°. This was then repeated with an orthogonal (100)  
307 section, rotating the crystal such that E//[010] and E//[001]. Polar plots are presented  
308 in Figure 4.

309 As has been observed before (although not always interpreted as such), the absorption  
310 associated with [TiCh-PD] is strongly polarized with the maximum absorbance when  
311 E//[100] (Kitamura et al., 1987; Koch-Muller et al., 2006; Miller et al., 1987; Padrón-  
312 Navarta et al., 2014; Walker et al., 2007).

313 The orientation of the absorber associated with the [Mg] is perpendicular to that  
314 associated with [TiCh-PD] observed in the (010) plane. The strongest absorbance of  
315 [Mg] is observed when E//[001], in accordance with theoretical calculations (Balan et  
316 al., 2011, Crepisson et al. 2014).

317 [Ti-triv] is resolved into two peaks with opposite polarization; the strongest peak  
318 ( $3351\text{ cm}^{-1}$ ) shows strongest absorbance when E//[100] and the weaker peak is  
319 strongest when E//[001]. This is the first determination of polarization of this defect;  
320  $\text{Ti}^{3+}$  was not among the trivalent cations considered in the *ab-initio* modeling of  $\text{M}^{3+}$ -  
321  $\text{H}^+$  substitutions by Zhang and Wright (2010).

322 Using the known polarization of the defects, defect-specific correction factors can be  
323 determined to convert unpolarised absorbance measured in sections parallel to the

324 (010) face ( $\Sigma\text{Abs}_{(010)}$ ) to total absorbance (i.e. the sum of polarised spectra measured  
325 in three mutually perpendicular directions;  $\Sigma\text{Abs}$ ). The correction factors for each  
326 defect are:

327

$$\Sigma\text{Abs}_{[\text{Mg}]} = \text{Abs}_{[\text{Mg}](010)} \times 2.09 \quad (1)$$

328

$$\Sigma\text{Abs}_{[\text{TiCh-PD}]} = \text{Abs}_{[\text{TiCh-PD}](010)} \times 1.97 \quad (2)$$

329

$$\Sigma\text{Abs}_{[\text{Ti-triv}]} = \text{Abs}_{[\text{Ti-triv}](010)} \times 2.28 \quad (3)$$

330

331 Note that the correction factors for [Mg] and [TiCh-PD] are  $\sim 2$ ; this is a function of  
332 near zero absorbance parallel to [010].

333 Several calibrations exist to convert total integrated absorbance to a quantified  
334 hydrogen content usually either as ppm H<sub>2</sub>O by weight or atomic proportion of H  
335 relative to Si, e.g. H/10<sup>6</sup>Si. Most of these calibrations are assumed to apply to all OH  
336 in a given mineral, that is, they are “mineral-specific” (Bell et al., 2003; Withers et al.,  
337 2012) but there is evidence that different substitution mechanisms require different  
338 absorption coefficients (Kovács et al., 2010), or that there is a general relationship  
339 between wavenumber and absorption coefficient (Skogby and Rossmann, 1991,  
340 Libowitzky and Rossmann, 1997). In this study, we use the calibrations of Bell et al.  
341 (2003), Kovács et al (2010), Withers et al (2012), plus the calibration of Bell et al.  
342 (2003) with absorption coefficients modified based on the wavenumber of the  
343 absorber using the relationship determined by Libowitzky and Rossmann (1997).  
344 Absorption coefficients for the different defects observed in this study are presented  
345 in Table 1, showing the potential for a considerable range of water contents to be

346 extracted from a single measurement. Because the determination of these absorption  
347 coefficients is still a matter of debate, ‘water’ contents will be presented  
348 predominantly as unpolarised integrated absorbance measured in the (010) plane (i.e.  
349 values from equations 1-3 must be used to convert these values into total integrated  
350 absorbance). The calculated water contents (at the crystal edge) using these  
351 calibrations are given in Table 2 only. Importantly, the absorption coefficients do not  
352 affect diffusion coefficients – diffusion in this system is independent of the  
353 concentration of diffusing hydrogen, nor do they affect calculations based on *relative*  
354 concentrations of the same defect in different experiments.

355

#### 356 **Interface OH concentrations**

357

358 The concentrations of OH extrapolated to the crystal/fluid interface should be the  
359 equilibrium concentrations towards which diffusion progresses. In these experiments  
360 this interface concentration is not a global equilibrium but a metastable one (where  
361 ‘interface’ refers to the closest measurement to the crystal edge within the spatial  
362 resolution of FTIR in this configuration), determined by the initial state of the crystal  
363 as imposed during its preparation at 1500 °C. It should be noted that our ‘metastable  
364 equilibrium’ is not the same metastable equilibrium described in the classic work of  
365 Kohlstedt and Mackwell (1998) and recently discussed by Ferriss et al (2015), but still  
366 refers to the same type of situation – an apparent equilibrium that will be eliminated if  
367 anneals are conducted at higher temperatures or for longer times. This is discussed  
368 below in relation to the effect of oxygen fugacity on interface concentrations.

369 The total concentration of hydrous defects at the interface (i.e. the total integrated area  
370 of peaks in the OH region) increases exponentially as a function of increasing

371 temperature (Tables 2-3, Figure 5b). The [Ti-triv] and [Mg] defects show similar  
372 relationships (Figure 5a). The concentration of H associated with [TiCh-PD],  
373 however, changes only a little as temperature increases, with considerable scatter.  
374 The interface concentrations of all the defects increase with increasing pressure  
375 (Table 2; Figure 5b). Decreasing  $\alpha\text{SiO}_2$  leads to lower OH concentration at the  
376 interface, but the change is almost entirely taken up by [Ti-triv] (Figure 6; Tables 2-  
377 3).

378

### 379 **Treatment of diffusion profiles**

380

381 The intensity of the bands in the OH stretching region all decrease from the rim to the  
382 core of the crystals (e.g. Figure 7). As a preliminary treatment of the data, the  
383 integrated area under all three peak populations was summed together; this gives a  
384 simple indication of bulk diffusion rate without any consideration of defect specifics.  
385 These data (integrated area measured using unpolarised light as a function of distance)  
386 were then fitted to the solutions to Fick's second law for two boundary conditions.  
387 Where traverses were conducted across the entire length of the crystal and diffusion  
388 was symmetrical, concentration-distance profiles were fit to the solution for one-  
389 dimensional, concentration independent diffusion from an infinite source into a finite  
390 slab from Carslaw and Jaeger (1959); this is the same solution used by Demouchy and  
391 Mackwell (2003) in similar experiments:

392

$$C(x) = (C_{\text{rim}} - C_{\text{core}}) \cdot \left( \operatorname{erfc} \frac{x}{2\sqrt{Dt}} + \operatorname{erfc} \frac{X-x}{2\sqrt{Dt}} \right) + C_{\text{core}} \quad (4)$$

393 Where the analytical traverse only covered a small portion of the crystal, i.e. where  
394 the diffusion distances were very short or the diffusion was asymmetrical, the simple  
395 equation for one-dimensional diffusion into a semi-infinite slab was used (e.g., Crank  
396 1975):

397

$$C(x) = (C_{\text{rim}} - C_{\text{core}}) \cdot \text{erfc} \frac{x}{2\sqrt{Dt}} + C_{\text{core}} \quad (5)$$

398

399 In these equations,  $C(x)$  is the concentration of the diffusant at position  $x$ ,  $C_{\text{rim}}$  is the  
400 equilibrium (interface) concentration,  $C_{\text{core}}$  is the background (initial) concentration,  
401  $\text{erfc}$  is the complimentary error function,  $X$  (in (4)) is the total length of the profile  
402 (edge to edge of the crystal) in metres,  $D$  is the chemical diffusion coefficient (in  $\text{m}^2\text{s}^{-1}$ )  
403 and  $t$  is the duration of the experiment, in seconds. The  $C_{\text{core}}$  term is necessary given  
404 that some profiles showed non-zero water contents in the core – probably related to a  
405 contribution from diffusion along the third axis ([010], the  $b$  axis) of the cube.

406 In all experiments, the total integrated absorbance in the OH region (sum of all  
407 defects) could be satisfactorily fitted to these equations. The results are presented in  
408 Table 2 as  $\log D(\Sigma H)$  for H diffusion along both the  $a$  and  $c$  axes (i.e. [100] and  
409 [001]). The errors on  $\log D$  were determined manually using the estimated maximum  
410 and minimum values that allowed fits within the data scatter. Insofar as these  
411 uncertainties correspond to approximately 95% confidence limits, they should be  
412 approximately equivalent to two standard deviations.

413

414 **Defect specific diffusion**

415

416 With the exception of the ‘two-slope’ sides of asymmetrical profiles (discussed  
417 below), the integrated areas corresponding to each of the three substitution types  
418 could be individually fitted as a function of distance to equations ( 4 ) or ( 5 ). A map,  
419 plus extracted, fitted profiles from all defects along both the *a* and *c* axes is shown in  
420 Figure 8.

421 The results of curve-fitting are shown in Table 2. In all cases except perhaps  
422 experiment hydrol4 (2.5 GPa, 850 °C), the apparent diffusion coefficients of H  
423 associated with the three different defect substitution mechanisms overlap within  
424 error. In the hydrol4 experiment, the [TiCh-PD] concentration-distance profile is  
425 slightly longer than the profile associated with either [Ti-triv] or [Mg], but the  
426 difference between error bar tips is equivalent to only 0.1 in  $\log_{10}D$ . Notably, the  
427 anisotropy of H diffusion shown by the three defects is the same. In all cases,  
428 diffusion is faster along [001] than along [100].

429

#### 430 **Asymmetrical profiles**

431

432 All [001] profiles from 850 °C and 950 °C experiments show some asymmetry, with  
433 one side showing higher [TiCh-PD] and lower [Ti-triv] concentrations than the other.  
434 This behaviour is not observed in the 1000 °C experiment. Whether it is seen in the  
435 650 °C and 750 °C experiments is not clear; the hydroxyl concentrations are too low  
436 to resolve the behaviour of each defect.

437 In these profiles, the high [TiCh-PD]/low [Ti-triv] side shows concentration-distance  
438 profiles that cannot be fitted to the theoretical equations ( 4 ) or ( 5 ). This side of the  
439 profile is also associated with a low, sharp peak at 3428  $\text{cm}^{-1}$ . An example of such a  
440 profile is shown in Figure 9; the relative [Ti-triv]:[TiCh-PD] defect ratio is

441 considerably different from one side of the crystal to the other. In such profiles, the  
442 side where all defects can be individually fitted to equation ( 5 ) is termed ‘simple’  
443 and the side with higher [TiCh-PD] concentrations and mismatch to the theoretical  
444 diffusion equations is termed ‘two-slope’ given the clear break of slope in the profile.  
445 All further discussion of diffusion, except where explicitly referring to asymmetrical  
446 profiles, will address the ‘simple’ sides of the profiles. These anomalies may be  
447 related to non-stoichiometry caused by vapour loss, or perhaps some other  
448 contamination, introduced during the preparation of the crystal, which involved long  
449 annealing at very high temperatures. However, any detailed explanation would be  
450 speculative. Suffice it to note that, all diffusion coefficients reported here are taken  
451 from the other side of the crystals or determined from the sum of all defects (which  
452 always displays an error function shape).

453

#### 454 **H diffusion as a function of P, T, $a\text{SiO}_2$ and $f\text{O}_2$**

455

456 Neither  $f\text{O}_2$  nor  $a\text{SiO}_2$  have any influence on the rate of hydrogen diffusion, within  
457 error (Table 2, Figure 6). In the MgO buffered experiment, there is no visible Si  
458 vacancy substitution (i.e.  $\text{Mg}_2\text{H}_4\text{O}_4$ ), within the spatial resolution of FTIR.  
459 Although only two pressure conditions were investigated, the effect of pressure on the  
460 diffusion of hydrogen is constrained to be small (Figure 10, Table 2), and given the  
461 lack of outside-error difference in diffusion coefficients between the 1.5 GPa and 2.5  
462 GPa experiments, it is not possible to determine any activation volume of diffusion.  
463 Over the 350 °C temperature range investigated,  $\log_{10}D$  ( $c$ , total) increases by over  
464 three orders of magnitude (Figure 11). A similar change with temperature is seen for  
465 diffusion along [100]. Following Demouchy and Mackwell (2003), a global fit (using

466 least squares) was performed for [100] and [001] diffusion coefficients (total  
467 absorbance) to determine the activation energy ( $E_A$ ) and pre-exponential factor  $D_0$   
468 using the relationship  $D=D_0.\exp(E_A/RT)$  (i.e.  $\log_{10}D = \log_{10}D_0+(E_A/2.3RT)$ , where  
469 2.3 is the natural logarithm of 10). We assume that  $E_A$  is the same in each direction.  
470 The least-squares minimization gives a good fit to the data and yields the relationship:  
471

$$\log D(\Sigma H) = \log D_0(\Sigma H) + \left( \frac{-223(\pm 8) \text{kJmol}^{-1}}{2.3RT} \right) \quad (6)$$

472  
473 Where  $D_0[100] = -3.04 \pm 0.4$  and  $D_0[001] = -2.18 \pm 0.4$ , i.e. diffusion along [001] is one  
474 order of magnitude faster than along [100]. The fit is shown as solid black lines in  
475 Figure 11.

476

477

## 478 Discussion

479

### 480 Previous determinations of mechanisms and rates of hydrogen diffusion

481

482 The addition of positive charge caused by protonation must be charge-balanced by  
483 either diffusion-in of a negative species or diffusion-out of another positively charged  
484 species. Here we use the term “species” to refer to a point-defect identity that may be  
485 an ion either on a lattice site or interstitial, a vacancy in the lattice, or an electron or  
486 electron hole (polaron).

487 Conceptually, it might seem reasonable that the fastest mechanism of H diffusion in  
488 natural olivine is one in which involves the smallest, lightest species, i.e. where

489 charge-balance is achieved by reducing pre-existing  $\text{Fe}^{3+}$  to  $\text{Fe}^{2+}$  (Kohlstedt and  
490 Mackwell, 1998; Mackwell and Kohlstedt, 1990). The reduction of  $\text{Fe}^{3+}$  can be  
491 thought of as eliminating polarons (electron holes), thus this mechanism may be  
492 described as proton-polaron exchange. This mechanism depends on the presence of  
493 initial  $\text{Fe}^{3+}$ , whose concentration in natural olivine is only at the tens to hundreds of  
494 ppm level (e.g. Dohmen and Chakraborty, 2007; Mallmann and O'Neill, 2009).  
495 A slower mechanism (although still extremely fast when compared to Mg, Si and O  
496 diffusion in olivine) uses M-site (octahedral, magnesium/iron site) vacancies for  
497 charge balance (e.g. Demouchy and Mackwell, 2003; Demouchy and Mackwell,  
498 2006). The coupled diffusion-in of a vacancy and two protons necessarily removes  
499 Mg from the crystal, hence this mechanism should depend on chemical potentials; if  
500 Mg is lost then the reaction should be favoured at low activity of magnesia ( $\text{MgO}$ ).  
501 Diffusion along this path is anisotropic; fastest along the  $c$  ([001]) crystallographic  
502 axis, relating to the presence of tightly spaced M-site chains along this direction  
503 (Demouchy and Mackwell, 2003).  
504 The last mechanism that does not involve some coupled substitution with an alien  
505 cation involves vacant tetrahedral sites ( $\text{Si}^{4+}$  sites) charge-balanced by four protons.  
506 Diffusion along this pathway is likely to be close to isotropic; the tetrahedral sites are  
507 relatively evenly spaced in different crystallographic directions. This mechanism  
508 displaces silicon from the crystal, so is expected to have the opposite dependence on  
509 chemical potentials as the M-site pathway. This was recently studied in terms of  
510 hydrogen diffusion-out by Padrón-Navarta et al. (2014) and found to be orders of  
511 magnitude slower than diffusion involving M-site vacancies.

512

513 **Defect formation and diffusion mechanisms – this study**

514  
515 In this and the following sections, equilibria involving point defects will be presented  
516 in Kröger-Vink notation, as has become conventional. In this notation, the main  
517 letters represents the species (e.g., Mg = magnesium, Ti = titanium, V = vacancy),  
518 subscript is the site location (Mg=octahedral [assume pure forsterite], Si=tetrahedral,  
519 O=oxygen, i=interstitial) and superscript is charge excess or deficiency on the site  
520 (<sup>x</sup>=no charge excess/deficiency, <sup>'</sup>=single charge deficiency, <sup>\*</sup>=single charge excess). A  
521 neutral charge exists when the tetrahedral site contains a 4+ cation, octahedral 2+,  
522 oxygen 2- and interstitial 0. Following Walker et al (2007), coupled defects (i.e.  
523 coupled for charge balance) are contained within curly braces. Herein, following  
524 Ingrin and Blanchard (2006), a fully protonated M-site vacancy is notated  
525  $\{V_{Mg}^{//} + 2H_i^*\}$ , i.e. M-site vacancy charge-balances the protons on interstitial sites.  
526 Without detailed structural knowledge, which might be obtainable by modeling (e.g.,  
527 Balan et al, 2011, Walker et al. 2007, Crepisson et al. 2014), claiming specific site  
528 occupancies for the H substitutions is dubious. For simplicity, the latter substitution  
529 could also be written as  $(2H)_{Mg}^x$ , assuming that the two protons are directly on the M-  
530 site (this is unlikely to be correct), or, probably most accurately,  $\{V_{Mg}^{//} + 2OH_O^*\}$ , with  
531 the hydrogen associated with nearby oxygen. The actual positions of the H have no  
532 effect on the stoichiometry of the point-defect reactions.  
533 To understand the diffusion of H through Nominally Anhydrous Minerals, three types  
534 of reactions must be considered. Firstly, there is the formation of defects at the crystal  
535 edge, which represent the equilibrium situation and should give the equilibrium  
536 concentrations of the defects at the conditions of T, P and chemical potentials  
537 imposed in the experiments. In these reactions, free H<sub>2</sub>O, MgO, O<sub>2</sub> etc are permissible  
538 components. Using our analytical technique, we do not see the true interface, but the

539 near interface region, which is then extrapolated back to the crystal edge. The second  
540 reaction type describes the movement of species through the crystal, which is  
541 responsible for the macroscopic diffusion. The third type of reaction is akin to order-  
542 disorder reactions in crystals, and describes the reaction between one kind of hydrous  
543 defect with an anhydrous component to produce another kind of hydrous defect. As  
544 such reactions involve transfer only on the unit-cell scale, usually they may be  
545 expected to be fast relative to the macroscopic transport of material through crystals,  
546 but this need not always be the case, and perhaps such exchange reactions could on  
547 occasion be rate-limiting.

548 The crystal chemistry of the Ti in the starting material, which was synthesized at 1500  
549 °C under anhydrous conditions, can be deduced from previous work. Hermann et al.  
550 (2005) showed that the substitution of  $\text{Ti}^{4+}$  in olivine under anhydrous conditions and  
551 in the absence of charge-balancing by aliovalent impurities such as  $\text{Al}^{3+}$  or  $\text{B}^{3+}$  occurs  
552 as  $\text{Mg}_2\text{Ti}^{4+}\text{O}_4$ , with  $\text{Ti}^{4+}$  substituting for  $\text{Si}^{4+}$  on the tetrahedral site (see also Walker et  
553 al. 2007).

554 Jollands et al. (submitted) postulated that the substitution of Ti in olivine in the  
555 (anhydrous) experimental conditions used in the Ti-doping stage can be described by  
556  $\text{Mg}_2\text{Ti}^{4+}\text{O}_4$  and  $(\text{Ti}_{4/3}^{3+}[\text{vac}]_{2/3})\text{SiO}_4$ , that is,  $\text{Ti}^{4+}$  on the T-sites and  $\text{Ti}^{3+}$  on the M sites  
557 charge balanced by M-site vacancy ([vac]). This was inferred based on a relationship  
558 between Ti diffusion and  $f\text{O}_2$  (diffusivity as a function of  $f\text{O}_2$  followed a sigmoidal  
559 pattern consistent with a one electron transfer reaction), characteristic diffusion  
560 profile shapes related to  $\text{Ti}^{4+}$  being ‘trapped’ on the T-sites (stepped diffusion profiles  
561 at high  $f\text{O}_2$ , suggesting that the diffusing species [ $\text{Ti}^{4+}$ ] has two possible site locations  
562 with different diffusivities [T and M]) and FTIR analysis of hydroxylated diffusion  
563 profiles. At the T- $f\text{O}_2$  conditions of Ti doping, the equilibrium amount of  $\text{Ti}^{3+}/\Sigma\text{Ti}$  is

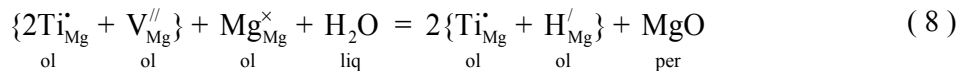
564 around half (Mallmann and O'Neill, 2010), and the Jollands et al. study (submitted)  
565 suggests that  $\text{Ti}^{3+}$  is favoured over  $\text{Ti}^{4+}$  by the kinetic nature of doping by diffusion.  
566 The FTIR spectra suggest that the three main OH substitutions are [TiCh-PD], [Ti-  
567 triv], and [Mg]. [Ti-triv] and [Mg] are associated with an M-site vacancy, whereas  
568 [TiCh-PD] involves a T-site vacancy. Nevertheless, the concentration-distance  
569 profiles of the substitution mechanisms have the same length (estimated) in each  
570 experiment, in each crystallographic orientation. At first glance, this might seem  
571 surprising, as the rates of both major-element diffusion (e.g. Chakraborty, 1997;  
572 Chakraborty et al., 1994; Dohmen et al., 2002) and hydrogen diffusion (Demouchy  
573 and Mackwell, 2003; Padrón-Navarta et al., 2014) are orders of magnitude slower on  
574 the T-site than M-site.  
575 This can be explained, however, by considering the formation reactions of these  
576 defects. It becomes clear, below, that these concentration-distance profiles are, in fact,  
577 the products of both diffusion (that is, macroscopic movement of H through the  
578 crystal) plus point-defect reactions that operate on the unit-cell length scale.  
579 In order to form [Mg] at the interface, Mg exchanges with two hydrogen ions:

580



581

582 Then, the defect moves by cation-vacancy exchange of  $\{ \text{V}_{\text{Mg}}^{\prime\prime} + 2\text{H}_i^{\bullet} \}$  for  $\text{Mg}_{\text{Mg}}^{\times}$ .  
583 Reaction ( 7 ) describes the formation of this defect at the interface, where there is a  
584 reservoir to buffer the chemical potentials (i.e., activities) of MgO and  $\text{H}_2\text{O}$ .  
585 Hydration of anhydrous  $\text{Ti}^{3+}$  defects requires hydrogen-vacancy exchange:



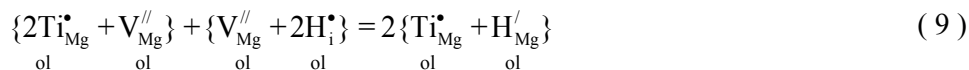
586 After formation, the defect can move by exchange of  $\underset{\text{ol}}{\text{V}}_{\text{Mg}}^{\prime\prime} + \underset{\text{ol}}{\text{Mg}}_{\text{Mg}}^{\times}$  for  $2\underset{\text{ol}}{\text{H}}_{\text{Mg}}^{\prime}$ .

587 Alternatively, interaction between the anhydrous  $\text{Ti}^{3+}$  defect (considered immobile

588 over the scale of these experiments) and  $[\text{Mg}]$  (highly mobile) can also form  $[\text{Ti-triv}]$

589 inside the crystal by redistribution of protons:

590



591

592 The choice of mechanism is not clear-cut, but in both cases diffusion of the defect (or

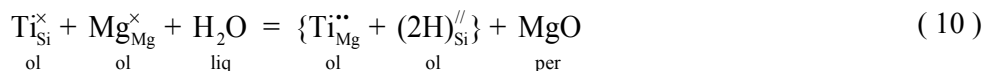
593 formation of the defect by vacancy diffusion and then reaction) is limited to the rate

594 of Mg-vacancy diffusion.

595 To form  $[\text{TiCh-PD}]$  from  $\text{Mg}_2\text{Ti}^{4+}\text{O}_4$  (anhydrous  $\text{Ti}^{4+}$ ) requires  $\text{Ti}^{4+}$  to move from the

596 tetrahedral to the octahedral site and be replaced by hydrogen. This necessarily

597 displaces magnesium:



598

599 In order for the defect to then diffuse through the crystal, the  $\{\underset{\text{ol}}{\text{Ti}}_{\text{Mg}}^{\bullet\bullet} + (2\underset{\text{ol}}{\text{H}})_{\text{Si}}^{\prime\prime}\}$  could

600 exchange places with an adjacent  $\underset{\text{ol}}{\text{Ti}}_{\text{Si}}^{\times} + \underset{\text{ol}}{\text{Mg}}_{\text{Mg}}^{\times}$ . However, this involves  $\text{Mg}^{2+}$  and  $\text{Ti}^{4+}$

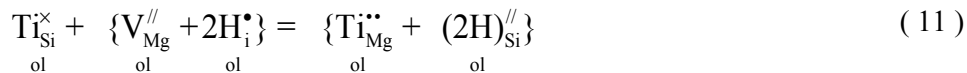
601 exchanging places on the M sites, which is expected to be slower than M-site vacancy

602 diffusion. This diffusion mechanism is not in agreement with the data, which shows

603 that H diffusion associated with the different defects have the same diffusion rate.

604 Alternatively,  $\underset{\text{ol}}{\text{Ti}}_{\text{Si}}^{\times}$  could interact with  $[\text{Mg}]$

605

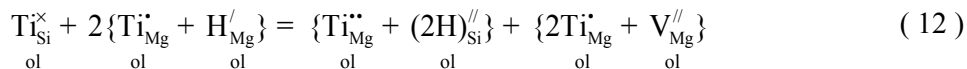


606

607 While these reactions involve the T-site, the macroscopic movement is on the M-site.

608 Or, the anhydrous  $\text{Ti}^{4+}$  defect could interact with two [Ti-triv], forming one [TiCh-

609 PD] and eliminating both [Ti-triv]:



610

611 For each [TiCh-PD] that is created from the anhydrous  $\text{Ti}^{4+}$  substitution, a different

612 hydroxylated defect must be available nearby, thus the diffusion rate of H along this

613 defect pathway should be similar to that of [Mg] or [Ti-triv].

614 Reaction ( 12 ) is considered more likely in these experiments, given that the

615 concentration of [Ti-triv] is so much higher than that of [Mg] (see Table 2).

616 That the three hydrated point defects observed in these experiments ([TiCh-PD], [Ti-

617 triv] and [Mg]) all propagate at the same rate through the Ti-doped forsterite is

618 explained by the three mechanisms using the same pathway, that of Mg-vacancy

619 diffusion. This interpretation is supported by the similar crystallographic anisotropy

620 of the concentration-distance profiles (longest profiles, hence fastest diffusion, along

621 [001] where M sites are most closely spaced).

622

623 **The effect of chemical activity on diffusion and apparent interface**624 **concentrations**

625

626 Two conditions of  $a\text{SiO}_2$  were investigated at 850 °C, 1.5 GPa, by packing the crystal

627 in either forsterite-enstatite or forsterite-periclase.

628 As forming all defects (excluding any direct substitution of  $4\text{H}^+$  for  $\text{Si}^{4+}$ ; not seen in  
629 these experiments) at the interface necessarily liberates MgO (see reactions ( 10 ), ( 8  
630 ) & ( 7 )), it is expected that the hydrogen solubility in the two conditions should  
631 differ accordingly. Assuming that the pre-existing anhydrous point defects do not  
632 become fully saturated (i.e. fully hydroxylated), the concentrations of all point defects  
633 should be higher at higher  $a\text{SiO}_2$ , and indeed, this is the case (Table 1). At some  
634 temperature and pressure, the anhydrous defects should become effectively saturated,  
635 then this relationship should no longer hold.

636 This relationship between  $a\text{SiO}_2$  and interface concentration is in line with the effect  
637 of  $a\text{SiO}_2$  on Zr and Hf interface concentrations in olivine in similarly buffered  
638 diffusion experiments – higher concentrations at higher  $a\text{SiO}_2$  (see Jollands et al.,  
639 2014).

640 However, the  $a\text{SiO}_2$  of the buffer does not affect the rate of H diffusion. This is in  
641 contrast to the effect of  $a\text{SiO}_2$  on the diffusion of Zr, Hf, Ni and Co in olivine, where  
642 higher  $a\text{SiO}_2$  consistently led to faster diffusion (Jollands et al., 2014; Zhukova et al.,  
643 2014). This relates to the substitution mechanism of  $\text{H}^+$  into the forsterite crystal  
644 structure. Given that the diffusing point defect is either  $\{\text{V}_{\text{Mg}}^{\prime\prime} + 2\text{H}_i^{\bullet}\}$  or  $\{\text{Ti}_{\text{Mg}}^{\bullet} + \text{H}_{\text{Mg}}^{\prime}\}$   
645 (which can also be written  $\{\text{Ti}_{\text{Mg}}^{\bullet} + \text{V}_{\text{Mg}}^{\prime\prime} + \text{H}_i^{\bullet}\}$ ), the diffusing hydrogen is always  
646 associated with an M-site vacancy. In the case of Zr, Hf, Ni and Co diffusion, the M-  
647 site vacancy population of the crystal, whose concentration was imposed by the  
648 external buffering assemblage, provided the mechanism for diffusion (i.e. cation-  
649 vacancy exchange). In the case of  $\text{H}^+$ , the diffusing cation is already associated with  
650 its own vacancy. In short, this means that the  $\text{H}^+$  does not need to wait for a  
651 randomly-walking M-site vacancy in order to make a diffusive jump, hence the

652 overall vacancy concentration of the crystal (imposed by the  $a\text{SiO}_2$  buffer) does not  
653 appreciably affect the diffusion rate.

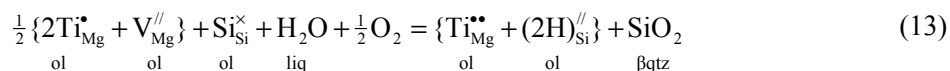
654

655 **The effect of  $f\text{O}_2$  on interface concentrations**

656 The starting crystal was prepared at very low oxygen fugacity, where Ti substitutes  
657 predominantly in the 3+ oxidation state (Jollands et al., submitted). The conditions  
658 under which the hydroxylation were performed (either Re-ReO<sub>2</sub> or Ag-Ag<sub>2</sub>O) were  
659 very oxidizing, where there should be no detectable Ti<sup>3+</sup> at equilibrium (e.g.,  
660 Mallmann and O'Neill, 2009). Yet, after hydroxylation, hydrated Ti<sup>3+</sup> is the main  
661 hydrous substitution regardless of  $f\text{O}_2$  in all the FTIR spectra (except the anomalous  
662 “two-slope” profiles), greatly exceeding the amount of Ti<sup>4+</sup> forming the TiCh-PD.  
663 Even in the two-slope profiles where some Ti<sup>3+</sup> is thought to have been oxidized, the  
664 Ti<sup>3+</sup> amount remains high.

665 The reason for this is that oxidation of anhydrous Ti<sup>3+</sup> to hydrous Ti<sup>4+</sup> (as [TiCh-PD])  
666 requires considerable site rearrangement, and the expulsion of Si:

667



668

669 Evidently, these kinetics do not allow the Ti<sup>3+</sup>/ΣTi ratio (at the interface, within the  
670 resolution of FTIR spectroscopy) to reach equilibrium; this ratio should be nearly zero  
671 at the experimental conditions. It is expected that longer experimental times and/or  
672 higher temperatures should allow equilibration of the point defects with the externally  
673 buffered conditions, and indeed this has been seen in a similar system (Cr<sup>3+</sup> and Cr<sup>4+</sup>  
674 in forsterite; Jollands et al., 2015).

675

676 **Comparison with other studies**

677

678 Several other studies have determined H diffusion coefficients along various  
679 pathways in olivine; these are shown in Figure 11 alongside the Arrhenius curves  
680 from this study.

681 Given that the mechanisms observed in this study are all interpreted as related to the  
682 rate of [Mg] diffusion, it might be expected that the diffusion coefficients of this study  
683 should overlap on the Arrhenius plot with those found by Demouchy and Mackwell  
684 (2003). However, in the 900-1000 °C range where experiments from this and their  
685 study overlap, the diffusion coefficients are around 0.5 orders of magnitude faster in  
686 this study. This discrepancy is, however, small given the overall variation of H  
687 diffusion in olivine found in the literature. The experiments of Demouchy and  
688 Mackwell (2003) were conducted at much lower pressure (using cold-seal apparatus  
689 rather than piston cylinder), but the lack of any dependence of pressure on diffusion in  
690 this study argues that this should not be significant. Given that H diffuses with its own  
691 vacant M-site (i.e. interstitial mechanism), the concentration of M-site vacancies  
692 should not affect the rate of diffusion (shown by no effect of  $a\text{SiO}_2$  on the diffusion  
693 rate). This suggests that the slight increase in diffusion rate relative to that of  
694 Demouchy and Mackwell (2003) is not due to the relatively high M-site vacancy  
695 concentration related to  $\text{Ti}^{3+}$ .

696 Padrón-Navarta et al. (2014) synthesised Ti-doped forsterite under hydrous  
697 conditions, which were also relatively oxidized, to produce a starting material with H  
698 predominantly in [TiCh-PD] and hydroxylated T-vacancies, with minor [Mg] and  
699 [triv], which may have been due to minor  $\text{Ti}^{3+}$ . They then diffused the H out of the  
700 crystals at atmospheric pressure, which was monitored not by measuring diffusion

701 profiles (as in this study), but by determining the H associated with each defect type  
702 in the bulk crystal. Their results showed that [Mg] and [triv] disappeared rapidly, with  
703 implied diffusion rates similar to those found by Demouchy and Mackwell (2003) and  
704 in this study (Figure 11). [TiCh-PD], however, were eliminated more slowly, with  
705 implied diffusion rates over an order of magnitude slower than in this study (Figure  
706 11). Padrón-Navarta et al. (2014) also found that after [TiCh-PD]s were eliminated,  
707 the rate of decrease of the hydroxylated T-site defects almost ceased. Their study thus  
708 showed that the rate of diffusion of H out of the crystals was dependent on the fastest  
709 available mechanism. After the elimination of the (presumed) [triv] defects, there is  
710 no mechanism to transfer the [TiCh-PD] locally to a fast diffusion mechanism (i.e.,  
711 the reverse of reaction ( 12 )), which explains the apparently slower rate of diffusion.  
712 This assertion could be tested by measuring H diffusion into forsterite doped with  
713 small amounts of  $Ti^{4+}$  and no  $Ti^{3+}$  or other trivalent cations if such material were to  
714 become available. We expect that in the absence of any hydroxylated trivalent defects,  
715 H diffusion (diffusion-in) along the [TiCh-PD] pathway would be considerably slower  
716 than observed in this study.

717

## 718 **Implications**

719

- 720 1. Hydrogen diffusion is slightly faster in Ti-doped forsterite than in pure  
721 forsterite. The presence in natural olivines of trace elements with an affinity  
722 for  $H^+$  (e.g. trivalent cations on the M-sites) should be considered when  
723 projecting experimentally determined diffusion coefficients into natural  
724 systems.

- 725 2. The chemical activity and oxygen fugacity of the surroundings does not affect  
726 the rate of H-diffusion in olivine, along the M-site pathway. Frozen H-  
727 diffusion profiles in natural xenocrysts can be used to determine timescales of  
728 residence/ascent regardless of the silica saturation or undersaturation of the  
729 magma.
- 730 3. Diffusion in systems that require charge balance is a composite problem of  
731 both (a) *diffusion* of vacancies/charge-balancing agents and the diffusing  
732 species and (b) *reactions* resulting in rearrangement of site occupancy. Whilst  
733 diffusion-in (from this study) and diffusion-out (from Padrón-Navarta et al.,  
734 2014) coefficients are significantly different, no different *diffusion*  
735 mechanisms are needed to describe this. The difference in apparent *diffusion*  
736 rates is instead a function of the difference in *reaction* mechanisms. In systems  
737 that require charge-balance, it may be necessary to consider both diffusion and  
738 reaction when attempting to describe diffusion rate.

739

#### 740 **Acknowledgements**

741 The authors wish to thank Rachel Stott and Pete Tollan for early assistance with FTIR  
742 spectroscopy, Jeremy Wykes, Jung Woo Park, Maria Rosa Scicchitano, Michael  
743 Schwartz, Dave Clark and Dean Scott for various general help, Uli Faul and Andrew  
744 Berry for useful comments regarding Ti clinohumite defects, and Colin MacRae of  
745 CSIRO for providing OpticalFit software. The manuscript was greatly improved  
746 through constructive reviews by Elizabeth Ferriss and an anonymous reviewer, with  
747 editorial handling by Thomas Mueller.

748

749

Calibration used	Absorption coefficient		
	[TiCh-PD]	[Ti-triv]	[Mg]
Bell et al. (2003)	0.188 ± 0.012	0.188 ± 0.012	0.188 ± 0.012
Kovács et al. (2010)	0.18 ± 0.07	0.18 ± 0.05	0.03 ± 0.03
Bell et al (2003) & Libowitzky and Rossmann (1997)	0.188 ± 0.012	0.083 ± 0.014	0.056 ± 0.009
Withers et al. (2012)	0.119 ± 0.006	0.119 ± 0.006	0.119 ± 0.006

750

751 Table 1: Different determinations of absorption coefficients can have a considerable effect on  
 752 calculations of the concentration of H<sub>2</sub>O. Bell et al (2003) assume all defects have the same coefficient,  
 753 but their samples were dominated by defects in the [TiCh-PD] wavenumber range. Kovács et al (2010)  
 754 does not make this assumption but did not include absolute (standardless) measurements of hydrogen  
 755 concentration. Their samples included defects in the [Mg] and [TiCh-PD] range, along with trivalent  
 756 cation associated H (using Sc<sup>3+</sup>). Withers et al (2012) assumes the same coefficient for all defects, with  
 757 synthetic crystals dominated by bands in the [TiCh-PD] and [Mg] wavenumber range (although their  
 758 spectra were dominated by [Si] defect bands). Also given is the Bell et al (2003) coefficient (assumed  
 759 correct for [TiCh-PD] adjusted for lower wavenumbers using the Libowitzky and Rossmann (1997)  
 760 relationship. Considerable uncertainty still exists in absorption coefficients, hence in this study we refer  
 761 primarily to the integrated peak area rather than wt. ppm H<sub>2</sub>O.

762

I.D. (this study)	I.D. (SESAR)	T (°C)	P (GPa)	t (hr)	fO <sub>2</sub> buffer	aSiO <sub>2</sub> buffer	Sample thickness (µm)	log <sub>10</sub> diffusion coefficients (m <sup>2</sup> s <sup>-1</sup> )					Normalised Integrated absorbance at interface (cm <sup>-2</sup> )		
								logD <sub>[001]</sub> [TiCH-PD]	logD <sub>[001]</sub> [Ti-triv]	logD <sub>[001]</sub> [Mg]	logD <sub>[001]</sub> (total)	logD <sub>[100]</sub> (total)	[TiCh-PD]	[Ti-triv]	[Mg]
hydrol8	IEMC J0007	650	1.5	360	Re-ReO <sub>2</sub>	fo-ens	448±20	N.D.	-14.8 ±0.1	N.D.	-14.8 ±0.1*	-15.8 ±0.2*	12 ± 2	7.7 ± 0.7	N.D.
hydrol2	IEMC J0002	750	1.5	24	Re-ReO <sub>2</sub>	fo-ens	261±14	N.D.	-14.0 ±0.3	N.D.	-14.0 ±0.3*	N.D.	N.D.	0.2 ± 0.2	N.D.
hydrol1	IEMC J0001	850	1.5	6	Re-ReO <sub>2</sub>	fo-ens	567±10	-12.4 ±0.1	-12.4 ±0.1	-12.5 ±0.2	-12.5 ±0.1	-13.5 ±0.1	18 ± 1	51 ± 7	9 ± 4
hydrol6	IEMC J0005	850	1.5	12	Ag-Ag <sub>2</sub> O	fo-ens	536±10	-12.3 ±0.1	-12.6 ±0.1	-12.4 ±0.1	-12.5 ±0.1	-13.3 ±0.1	16 ± 1	51 ± 4	6 ± 0.5
hydrol7	IEMC J0006	850	1.5	12	Re-ReO <sub>2</sub>	fo-per	652±17	-12.6 ±0.1	-12.6 ±0.2	-12.7 ±0.1	-12.5 ±0.1		14 ± 2	28 ± 2	7 ± 1
hydrol4	IEMC J0004	850	2.5	12	Re-ReO <sub>2</sub>	fo-ens	605±16	-12.3 ±0.1	-12.6 ±0.1	-12.7 ±0.2	-12.6 ±0.1	-13.4 ±0.1	29 ± 5	81 ± 12	28 ± 5
hydrol3	IEMC J0003	950	1.5	3	Re-ReO <sub>2</sub>	fo-ens	499±12	-12.0 ±0.2	-11.9 ±0.1	-11.8 ±0.1	-11.9 ±0.2	-12.8 ±0.2	28 ± 3	74 ± 5	21 ± 2
hydrol10	IEMC J0008	1000	1.5	1	Re-ReO <sub>2</sub>	fo-ens	436±12	-11.4 ±0.1	-11.5 ±0.1	-11.6 ±0.1	-11.5 ±0.2	-12.1 ±0.2	20 ± 10	102 ± 2	31 ± 2

763

764 Table 2: Experimental conditions and results. Thicknesses are average and 1 standard deviation of thicknesses determined from all points measured in the crystal. SESAR ID  
 765 are International Geo Sample Numbers (IGSNs) compiled at <http://www.geosamples.org>. The diffusion coefficients (all log<sub>10</sub>D) are determined from summed absorbance  
 766 (sum of integrated areas from all three defects). Diffusion rates are determined along the [001] (logD<sub>[001]</sub>) and [100] (logD<sub>[100]</sub>) axes, all measured in the (010) plane using  
 767 unpolarised light. Integrated absorbance values are taken looking down the [010] direction. No correction is made for defect polarization – values corrected using Equations  
 768 1-3 are given in Table 3. Errors on diffusion coefficients and integrated absorbance are (subjectively) determined from data scatter around error function, or 0.1, whichever is  
 769 greater. \*Diffusion coefficient determined using Ti<sup>3+</sup> peak only. N.D.: not determined, peak too small.

I.D. (this study)	Total normalized integrated absorbance at interface ( $\text{cm}^{-2}$ )			wt. ppm $\text{H}_2\text{O}$ (interface)			
	[TiCh-PD]	[Ti-triv]	[Mg]	B03	K10	W12	B03+ LR
hydrol8	24 ± 4	18 ± 2		7.7 ± 1.2	7.4 ± 2.7	4.9 ± 0.7	5.9 ± 1.1
hydrol2		0.5 ± 0.5		0.1 ± 0.1	0.1 ± 0.1	0.1 ± 0.1	0 ± 0
hydrol1	35 ± 2	116 ± 16	19 ± 8	32.1 ± 5.5	27.9 ± 9.6	20.3 ± 3.3	17.4 ± 3.2
hydrol6	32 ± 2	116 ± 9	13 ± 1	30.1 ± 3	27 ± 8.7	19.1 ± 1.7	16.3 ± 2.5
hydrol7	28 ± 4	64 ± 5	15 ± 2	19.9 ± 2.4	16.9 ± 5.8	12.6 ± 1.4	11.3 ± 2
hydrol4	57 ± 10	185 ± 27	59 ± 10	56.5 ± 9.7	45.3 ± 16.6	35.7 ± 6	29.3 ± 6.2
hydrol3	55 ± 6	169 ± 11	44 ± 4	50.3 ± 5.2	41.6 ± 14	31.9 ± 3	26.8 ± 4.3
hydrol10	39 ± 20	233 ± 5	65 ± 4	63.3 ± 7.8	50.9 ± 18.1	40.1 ± 4.5	30.3 ± 7.6

770

771

772

773

774

775

776

777

778

779

780

781

782

783

784

785

786

787

788

789

790

791

792

793

794

795

796

797

798

799

800

801

802

803

804

805

806

807

808

809

810

811

812

813

814

815

816

817

Table 3: Interface total absorbance and  $\text{H}_2\text{O}$  concentration. Total normalized integrated absorbance values are corrected from those in Table 2 for orientation using the relationships presented in Equations 1-3, then converted into wt. ppm  $\text{H}_2\text{O}$  using the absorption coefficients detailed in Table 1.

Figure 1: Laser ablation ICP-MS transects across the starting material. The Ti profile has ~100 ppm variation from core to rim along [001]. Also note the change in Al concentration; Al shows a step from around 8 to 14 ppm. The dip in concentration at the centre of the [001] profile is from ablating over the pre-existing laser track along [100].

Figure 2: Experimental design. Top: schematic diagram of thick-walled, swaged Ag capsule containing a solid state  $f\text{O}_2$  buffer, a chemical activity buffer (forsterite + enstatite or periclase) and one or two oriented cubes of Ti-doped forsterite. Middle: capsule after experiment showing swelling; this suggests that pressure is hydrostatic inside the capsule, protecting the crystal from impingement or shearing. Bottom: transmitted light image of a double polished forsterite crystal post-experiment (hydrol1).

Figure 3: A spectrum from the infrared OH stretching (normalized to 1 cm thickness) region resolved into Gaussian distributions. Parameters a, b and c (inset table) reflect the position, width and height of the curves according to the Gaussian equation. The main peak at  $3351 \text{ cm}^{-1}$  is resolved into two, with a lower, slightly broader peak at  $3349 \text{ cm}^{-1}$  giving a lower wavenumber shoulder. The low peak at  $3252 \text{ cm}^{-1}$  is added to compensate for poor baseline subtraction in this region. Also shown are residuals between spectrum (black line) and simulation (red dotted line).

Figure 4: Left: Polarised, principal axis spectra taken from the interface ( $50 \times 50 \mu\text{m}$  aperture) of experiment hydrol 4 (2 perpendicular cuts), normalized to 1 cm thickness. Right: polar plots of each defect (three rows) taken in two perpendicular cuts (two columns). [TiCh-PD] is almost absent when the crystal is cut parallel to (100), hence this plot is missing. [Ti-triv] is comprised of two peaks with the opposite polarization.

800 Figure 5: Logarithm of integrated absorbance (unpolarised light, normalized to 1 cm  
801 thickness, not corrected for orientation) at the crystal edge as a function of inverse  
802 temperature. a) individual defects, all fo-ens buffered. [Ti-triv] and [Mg] show  
803 exponential increases, [TiCh-PD] does not. b) total absorbance. Oxygen fugacity does  
804 not affect interfaces but pressure and  $a\text{SiO}_2$  have an effect (850 °C data).

805 Figure 6: The effect of  $a\text{SiO}_2$  and  $f\text{O}_2$  on FTIR spectra (left) and diffusion profiles  
806 (right). The [Ti-triv] peak ( $3351\text{ cm}^{-1}$ ) remains, even in very oxidized conditions, with  
807 no change between Ag-Ag<sub>2</sub>O and Re-ReO<sub>2</sub> buffered conditions.

808 Figure 7: Variation in unpolarised IR spectra in the O-H stretching region across  
809 [001] of hydrol10 (1000 °C experiment). For clarity, this is a subsample (~25 %) of  
810 the total number of measurements from this axis. All spectra are normalized to 1cm  
811 thickness using integrated area of Si-O bands ( $1625\text{-}2150\text{ cm}^{-1}$ ) to eliminate artifacts  
812 from polishing on cloth (causing the crystal to be thinner at the edges).

813 Figure 8: Hydrol3 (950 °C experiment) mapped in unpolarised light with  $50\times 50\text{ }\mu\text{m}$   
814 aperture,  $30\text{ }\mu\text{m}$  step. Top: map of integrated area under trivalent peaks extracted from  
815 Bruker OPUS software, scaled between 0-90. The edge of the crystal appears white  
816 due to spectral contamination from epoxy resin. Middle: [001] profile extracted from  
817 map, including fits of integrated area underneath the [Ti-triv], [TiCh-PD] and [Mg]  
818 peaks to equation (4). Bottom: [100] profile extracted and treated in the same way.  
819 The large aperture and step size in mapping mode is not fully appropriate for such  
820 short profiles; diffusivity is underestimated.

821  
822 Figure 9: Example of an [001] profile (hydrol4) showing asymmetry. The right hand  
823 side of the profile allows fits to the error function for each individual defect. The left  
824 hand side does not; the steep inflection in [TiCh-PD] concentration at the interface  
825 precludes fits to a single error function. The left side of the profile also includes a  
826 short diffusion profile of a peak at  $3428\text{ cm}^{-1}$ . Interface spectra are also shown; the  
827 spectrum from the left has lower [Ti-triv] and higher [TiCh-PD] and [Mg] than the  
828 right hand spectrum, as well as the peak at  $3428\text{ cm}^{-1}$ . Also note that the left side  
829 suffers from a higher baseline in the [TiCh-PD] region.

830 Figure 10: The effect of pressure on diffusion along [001] and incorporation of  
831 hydrogen. From 1.5 to 2.5 GPa, the total OH solubility increases by 60-80 %. The  
832 concentration increase is taken up by [Mg] and [Ti-triv] defects; there is no increase  
833 in [TiCh-PD] concentration. Any change in the rate of diffusion with pressure is less  
834 than the uncertainty in the measurements.

835 Figure 11: Arrhenius plot of H diffusion in Ti-doped forsterite along the [001] (black  
836 circles) and [100] (grey circles). Solid black lines are fits to  $D=D_0\exp(E_a/RT)$ ,  
837 assuming that  $E_a$  (activation energy of diffusion) is the same along both axes. Also  
838 shown are data from M&K90: proton-polaron exchange; Mackwell and Kohlstedt  
839 (1990), DF12: H-D exchange, [100], natural olivine; DuFrane (2012), D&M(03):  
840 hydrogen- M-site vacancy coupled diffusion (forsterite); Demouchy and Mackwell  
841 (2003), D&M(06): hydrogen- M-site vacancy coupled diffusion (natural olivine);  
842 Demouchy and Mackwell (2006), I&B(06): H-D exchange, [001], near pure forsterite;  
843 Ingrin and Blanchard (2006). PN(14): Diffusion out of H from H±Ti doped forsterite;  
844 Padrón-Navarta et al. (2014).

845

846 **References**

847

- 848 Assal, J., Hallstedt, B., and Gauckler, L.J. (1997). Thermodynamic assessment of the silver–oxygen  
849 system. *Journal of the American Ceramic Society*, 80, 3054-3060.
- 850 Balan, E., Ingrin, J., Delattre, S., Kovács, I., and Blanchard, M. (2011) Theoretical infrared spectrum of  
851 OH-defects in forsterite. *European Journal of Mineralogy*, 23, 285-292.
- 852 Bell, D.R., and Rossman, G.R. (1992) Water in Earth's Mantle: The Role of Nominally Anhydrous  
853 Minerals. *Science*, 255, 1391-1397.
- 854 Bell, D.R., Rossman, G.R., Maldener, J., Endisch, D., and Rauch, F. (2003) Hydroxide in olivine: a  
855 quantitative determination of the absolute amount and calibration of the IR spectrum. *Journal of*  
856 *Geophysical Research: Solid Earth*, 108.B2.
- 857 Bell, D.R., Rossmann, G.R., and Moore, R.O. (2004) Abundance and Partitioning of OH in a High-  
858 pressure Magmatic System: Megacrysts from the Monastery Kimberlite, South Africa. *Journal of*  
859 *Petrology*, 45, 1539-1564.
- 860 Beran, A. (1969) Über (OH)-Gruppen in Olivin. *Oesterr Akad Wiss Math Naturwiss Kl Anzeiger*, 73-  
861 74 (in German).
- 862 Berry, A.J., Hermann, J., O'Neill, H.S.C., and Foran, G.J. (2005) Fingerprinting the water site in  
863 mantle olivine. *Geology*, 33, 869-872.
- 864 Berry, A.J., O'Neill, H.S.C., Hermann, J., and Scott, D.R. (2007a) The infrared signature of water  
865 associated with trivalent cations in olivine. *Earth and Planetary Science Letters*, 261, 134-142.
- 866 Berry, A.J., Walker, A.M., Hermann, J., O'Neill, H.S.C., Foran, G.J., and Gale, J.D. (2007b) Titanium  
867 substitution mechanisms in forsterite. *Chemical Geology*, 242, 176-186.
- 868 Bolfan-Casanova, N. (2005) Water in the Earth's mantle. *Mineralogical Magazine*, 69, 229-257.
- 869 Carslaw, H.S., and Jaeger, J.C. (1959) *Conduction of heat in solids*. Oxford: Clarendon Press, United  
870 Kingdom.
- 871 Chakraborty, S., Farver, J.R., Yund, R.A., and Rubie, D.C. (1994) Mg Tracer Diffusion in Synthetic  
872 Forsterite and San-Carlos Olivine as a Function of P, T and  $fO_2$ . *Physics and Chemistry of Minerals*,  
873 21, 489-500.
- 874 Chakraborty, S. (1997) Rates and mechanisms of Fe-Mg interdiffusion in olivine at 980 degrees-1300  
875 degrees C. *Journal of Geophysical Research-Solid Earth*, 102, 12317-12331.
- 876 Crank, J. (1975) *The Mathematics of Diffusion*. Oxford University Press, Oxford.
- 877 Creppisson, C., Bureau H., Blanchard M., Ingrin J., and Balan E. (2014) Theoretical infrared spectrum  
878 of partially protonated cationic vacancies in forsterite. *European Journal of Mineralogy*, 26, 203-210.
- 879 Demouchy, S., and Mackwell, S. (2003) Water diffusion in synthetic iron-free forsterite. *Physics and*  
880 *Chemistry of Minerals*, 30, 486-494.
- 881 Demouchy, S., Jacobsen, S.D., Gaillard, F., and Stern, C.R. (2006) Rapid magma ascent recorded by  
882 water diffusion profiles in mantle olivine. *Geology*, 34, 429-432.
- 883 Demouchy, S., and Mackwell, S. (2006) Mechanisms of hydrogen incorporation and diffusion in iron-  
884 bearing olivine. *Physics and Chemistry of Minerals*, 33, 347-355.
- 885 Demouchy, S., and Bolfan-Casanova, N. (2016). Distribution and transport of hydrogen in the  
886 lithospheric mantle: A review. *Lithos*, 240–243, 402-425.  
887
- 888 Denis, C.M., Demouchy, S., and Shaw, C.S. (2013) Evidence of dehydration in peridotites from Eifel  
889 Volcanic Field and estimates of the rate of magma ascent. *Journal of Volcanology and Geothermal*  
890 *Research*, 258, 85-99.

- 891 Dohmen, R., Chakraborty, S., and Becker, H.-W. (2002) Si and O diffusion in olivine and implications  
892 for characterizing plastic flow in the mantle. *Geophysical Research Letters*, 29, 2030.
- 893 Dohmen, R., and Chakraborty, S. (2007) Fe-Mg diffusion in olivine II: point defect chemistry, change  
894 of diffusion mechanisms and a model for calculation of diffusion coefficients in natural olivine (vol 34,  
895 pg 409, 2007). *Physics and Chemistry of Minerals*, 34, 597-598.
- 896 Du Frane, W.L., and Tyburczy, J.A. (2012) Deuterium-hydrogen exchange in olivine: Implications for  
897 point defects and electrical conductivity. *Geochemistry, Geophysics, Geosystems*, 13.
- 898 Ferriss, E., Plank, T., Walker, D., and Nettles, M. (2015). The whole-block approach to measuring  
899 hydrogen diffusivity in nominally anhydrous minerals. *American Mineralogist*, 100, 837-851.
- 900 Grant, K., Ingrin, J., Lorand, J.P., and Dumas, P. (2007) Water partitioning between mantle minerals  
901 from peridotite xenoliths. *Contributions to Mineralogy and Petrology*, 154, 15-34.
- 902 Hack, A.C., and Mavrogenes, J.A. (2006) A cold-sealing capsule design for synthesis of fluid  
903 inclusions and other hydrothermal experiments in a piston-cylinder apparatus. *American Mineralogist*,  
904 91, 203-210.
- 905 Hermann, J., Fitz Gerald, J.D., Malaspina, N., Berry, A.J., and Scambelluri, M. (2007) OH-bearing  
906 planar defects in olivine produced by the breakdown of Ti-rich humite minerals from Dabie Shan  
907 (China). *Contributions to Mineralogy and Petrology*, 153, 417-428.
- 908 Hirschmann, M.M., Aubaud, C., and Withers, A.C. (2005) Storage capacity of H<sub>2</sub>O in nominally  
909 anhydrous minerals in the upper mantle. *Earth and Planetary Science Letters*, 236, 167-181.
- 910 Jochum, K.P., Weis, U., Stoll, B., Kuzmin, D., Yang, Q., Raczek, I., Jacob, D.E., Stracke, A., Birbaum,  
911 K., Frick, D.A., Günther, D., and Enzweiler, J. (2011) Determination of Reference Values for NIST  
912 SRM 610–617 Glasses Following ISO Guidelines. *Geostandards and Geoanalytical Research*, 35, 397-  
913 429.
- 914 Jollands, M.C., O'Neill, H.S.C., and Hermann, J. (2014) The importance of defining chemical  
915 potentials, substitution mechanisms and solubility in trace element diffusion studies: the case of Zr and  
916 Hf in olivine. *Contributions to Mineralogy and Petrology*, 168, 1-19.
- 917 Jollands, M.C., O'Neill, H.S.C., Hermann, J., Berry A.J., and Rivard, C. (2015) Hydrogen Diffusion in  
918 Cr-Doped Forsterite Studied by XANES and FTIR. *Goldschmidt Abstracts*, 1470.
- 919 Kitamura, M., Kondoh, S., Morimoto, N., Miller, G.H., Rossman, G.R., and Putnis, A. (1987) Planar  
920 OH-bearing defects in mantle olivine. *Nature*, 328, 143-145.
- 921 Koch-Muller, M., Matsyuk, S., Rhede, D., Wirth, R., and Khisina, N. (2006) Hydroxyl in mantle  
922 olivine xenocrysts from the Udachnaya kimberlite pipe. *Physics and Chemistry of Minerals*, 33, 276-  
923 287.
- 924 Kohlstedt, D.L., and Mackwell, S.J. (1998) Diffusion of hydrogen and intrinsic point defects in olivine.  
925 *Zeitschrift für physikalische Chemie*, 207, 147-162.
- 926 Kovács, I., O'Neill, H.S.C., Hermann, J., and Hauri, E (2010) Site-specific infrared O-H absorption  
927 coefficients for water substitution into olivine. *American Mineralogist*, 95, 292-299.
- 928 Libowitzky, E., and Rossman, G. R. (1997). An IR absorption calibration for water in minerals.  
929 *American Mineralogist*, 82, 1111-1115.
- 930 Mackwell, S.J., and Kohlstedt, D.L. (1990) Diffusion of hydrogen in olivine: Implications for water in  
931 the mantle. *Journal of Geophysical Research: Solid Earth*, 95, 5079-5088.
- 932 MacRae, C.M., and Wilson, N.C. (2008) Luminescence database I: minerals and materials. *Microscopy  
933 and Microanalysis*, 14, 184-204.
- 934 Mallmann, G., and O'Neill, H.S.C. (2009) The Crystal/Melt Partitioning of V during Mantle Melting as  
935 a Function of Oxygen Fugacity Compared with some other Elements (Al, P, Ca, Sc, Ti, Cr, Fe, Ga, Y,  
936 Zr and Nb). *Journal of Petrology*, 50, 1765-1794.
- 937 Miller, G., Rossman, G., and Harlow, G. (1987) The natural occurrence of hydroxide in olivine.  
938 *Physics and Chemistry of Minerals*, 14, 461-472.
- 939 Padrón-Navarta, J.A., Hermann, J., and O'Neill, H.S.C. (2014) Site-specific hydrogen diffusion rates in  
940 forsterite. *Earth and Planetary Science Letters*, 392, 100-112.

- 941 Paton, C., Hellstrom, J., Paul, B., Woodhead, J., and Hergt, J. (2011) Iolite: Freeware for the  
942 visualisation and processing of mass spectrometric data. *Journal of Analytical Atomic Spectrometry*,  
943 26, 2508-2518.
- 944 Peslier, A.H., and Luhr, J.F. (2006) Hydrogen loss from olivines in mantle xenoliths from Simcoe  
945 (USA) and Mexico: Mafic alkalic magma ascent rates and water budget of the sub-continental  
946 lithosphere. *Earth and Planetary Science Letters*, 242, 302-319.
- 947 Peslier, A.H., Woodland, A.B., and Wolff, J.A. (2008) Fast kimberlite ascent rates estimated from  
948 hydrogen diffusion profiles in xenolithic mantle olivines from southern Africa. *Geochimica  
949 Cosmochimica Acta*, 72, 2711-2722.
- 950 Peslier, A.H., and Bizimis, M. (2015) Water in Hawaiian peridotite minerals: A case for a dry  
951 metasomatized oceanic mantle lithosphere. *Geochemistry, Geophysics, Geosystems*,  
952 doi:10.1002/2015GC005780
- 953 Peslier, A.H., Bizimis, M., and Matney, M. (2015) Water disequilibrium in olivines from Hawaiian  
954 peridotites: Recent metasomatism, H diffusion and magma ascent rates. *Geochimica Cosmochimica  
955 Acta*, 154, 98-117.
- 956 Pownceby, M. I., and O'Neill, H.S.C. (1994). Thermodynamic data from redox reactions at high  
957 temperatures. IV. Calibration of the Re-ReO<sub>2</sub> oxygen buffer from EMF and NiO+ Ni-Pd redox sensor  
958 measurements. *Contributions to Mineralogy and Petrology*, 118, 130-137.
- 959 Skogby, H., and Rossman, G.R. (1991). The intensity of amphibole OH bands in the infrared  
960 absorption spectrum. *Physics and Chemistry of Minerals*, 18, 64-68.
- 961 Shen, T., Hermann, J., Zhang, L., Padrón-Navarta, J.A., and Chen, J. (2014) FTIR spectroscopy of Ti-  
962 chondrodite, Ti-clinohumite, and olivine in deeply subducted serpentinites and implications for the  
963 deep water cycle. *Contributions to Mineralogy and Petrology*, 167, 1-15.
- 964 Smyth, J., Frost, D., Nestola, F., Holl, C., and Bromiley, G. (2006) Olivine hydration in the deep upper  
965 mantle: effects of temperature and silica activity. *Geophysical Research Letters*, 33.
- 966 Thoraval, C., and Demouchy, S. (2014) Numerical models of ionic diffusion in one and three  
967 dimensions: application to dehydration of mantle olivine. *Physics and Chemistry of Minerals*, 1-15
- 968 Umemoto, K., Wentzcovitch, R. M., Hirschmann, M. M., Kohlstedt, D. L., and Withers, A. C. (2011).  
969 first-principles investigation of hydrous defects and IR frequencies in forsterite: The case for Si  
970 vacancies. *American Mineralogist*, 96, 1475-1479.
- 971 Walker, A.M., Hermann, J., Berry, A.J., and O'Neill, H.S.C. (2007) Three water sites in upper mantle  
972 olivine and the role of titanium in the water weakening mechanism. *Journal of Geophysical Research:  
973 Solid Earth*, 112, B05211.
- 974 Wirth, R., Dobrzhinetskaya, L.F., and Green, H.W. (2001) Electron microscope study of the reaction  
975 olivine plus H<sub>2</sub>O+TiO<sub>2</sub> = titanian clinohumite plus Titanian chondrodite synthesized at 8 GPa, 1300 K.  
976 *American Mineralogist*, 86, 601-610.
- 977 Withers, A.C., Bureau, H., Raepsaet, C., and Hirschmann, M.M. (2012) Calibration of infrared  
978 spectroscopy by elastic recoil detection analysis of H in synthetic olivine. *Chemical Geology*, 334, 92-  
979 98.
- 980 Zhang, F., and Wright, K. (2010) Coupled (H<sup>+</sup>,M<sup>3+</sup>) substitutions in forsterite. *Geochimica  
981 Cosmochimica Acta*, 74, 5958-5965.
- 982 Zhang, Z., and Duan, Z. (2005) Prediction of the PVT properties of water over wide range of  
983 temperatures and pressures from molecular dynamics simulation. *Physics of the Earth and Planetary  
984 Interiors*, 149, 335-354.
- 985 Zhukova, I., O'Neill, H.S.C., Cambell, I.H., and Kilburn, M.R. (2014) The effect of silica activity on  
986 the diffusion of Ni and Co in olivine. *Contributions to Mineralogy and Petrology*, 168, 1-15.
- 987  
988
- 989

Figure 1

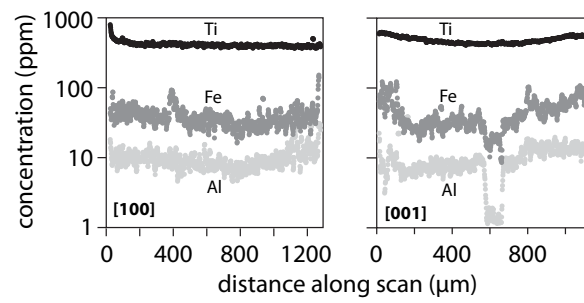


Figure 2

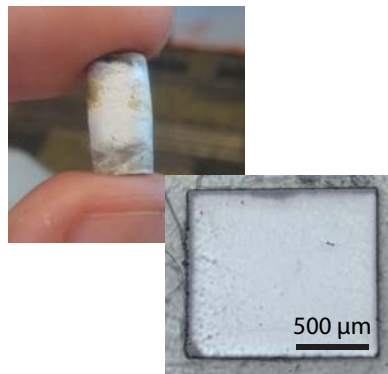
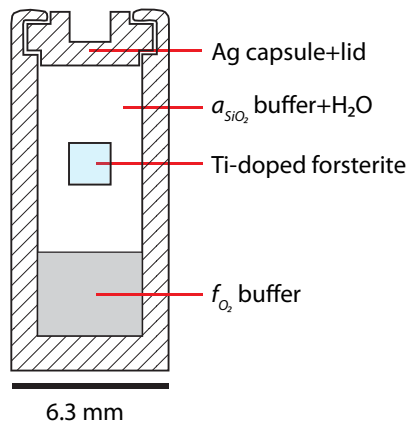


Figure 3

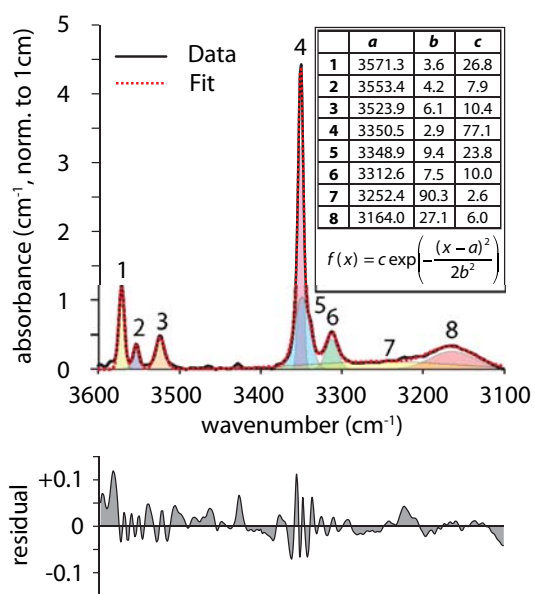


Figure 4

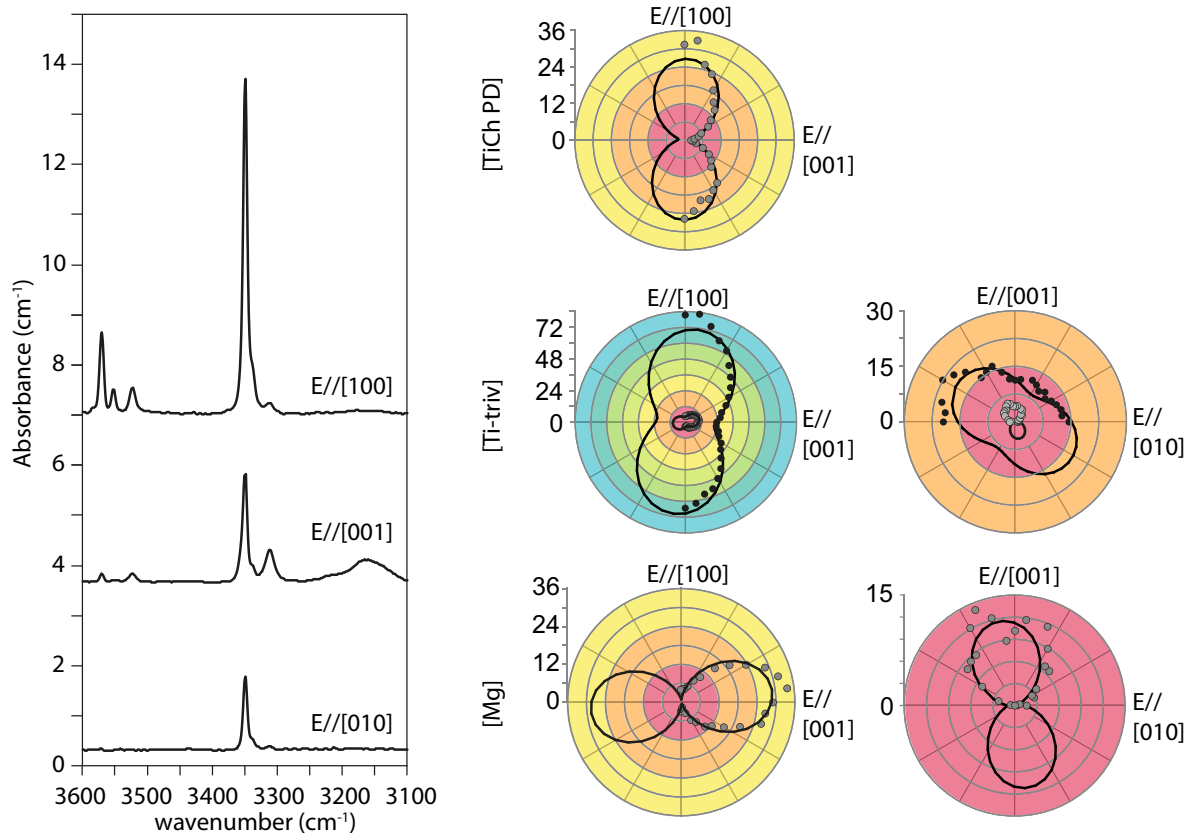


Figure 5

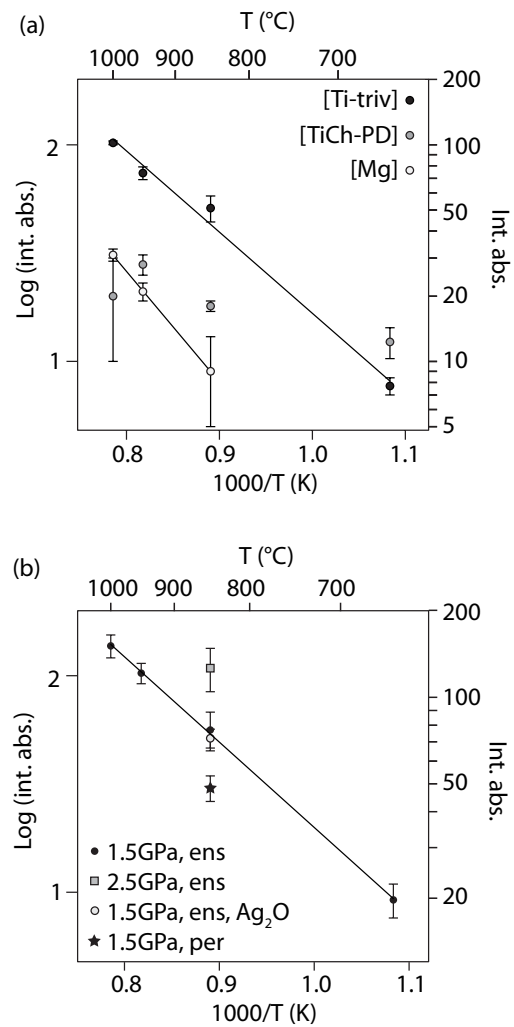


Figure 6

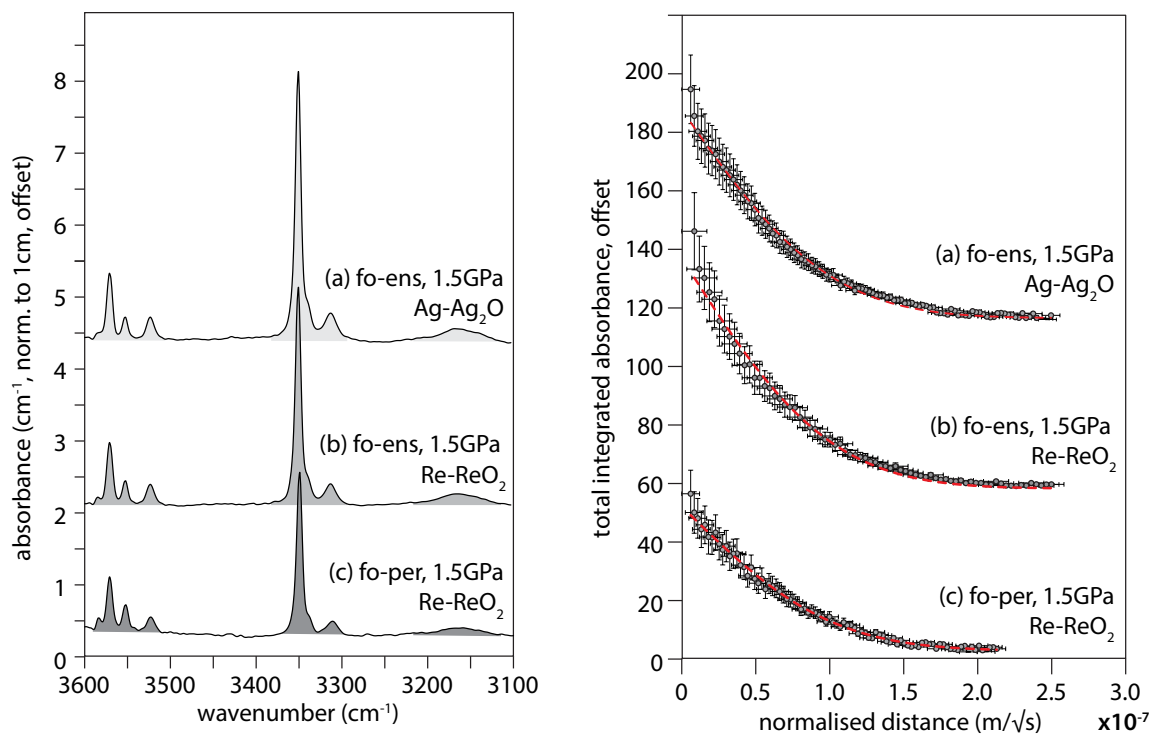


Figure 7

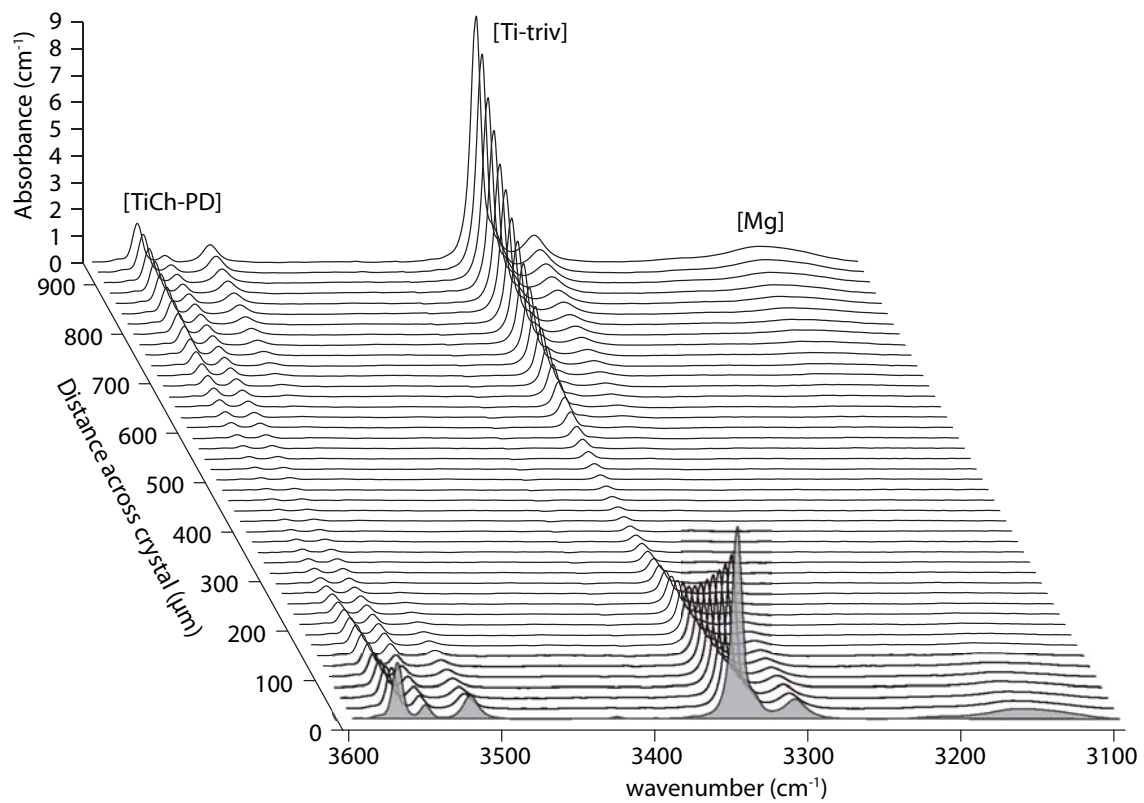


Figure 8

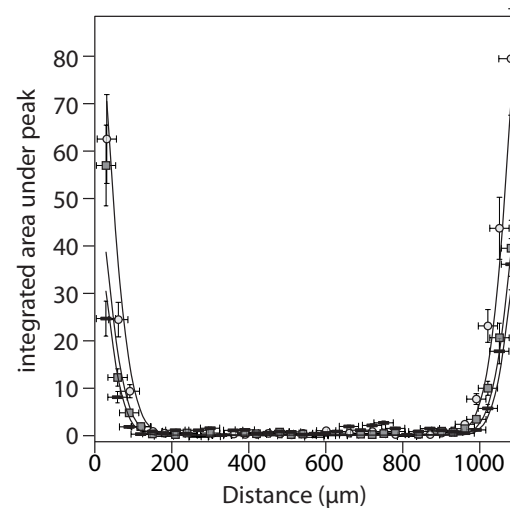
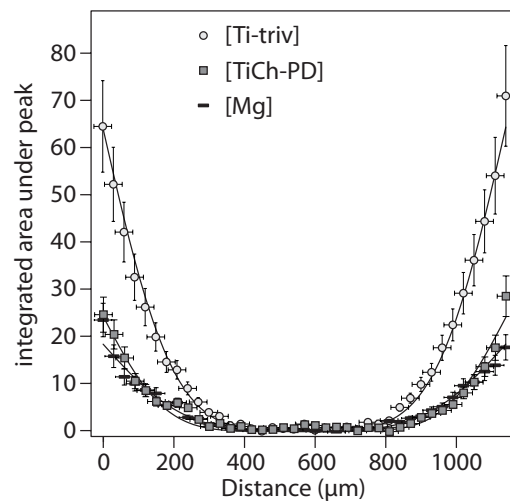
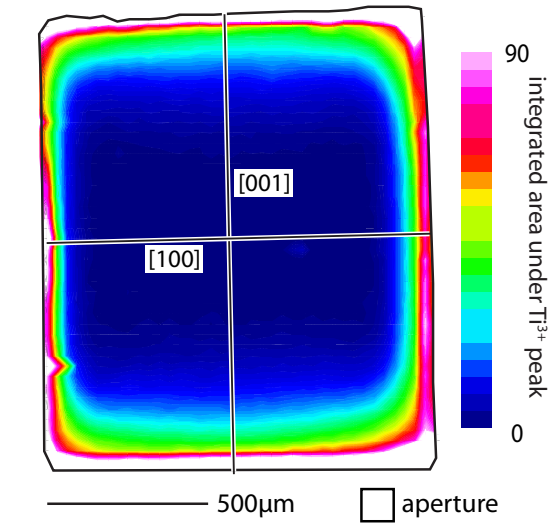


Figure 9

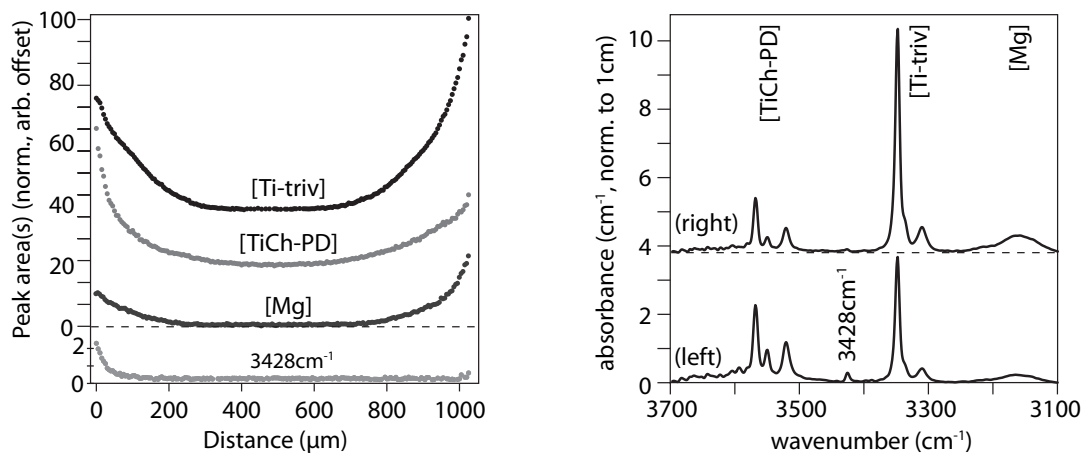


Figure 10

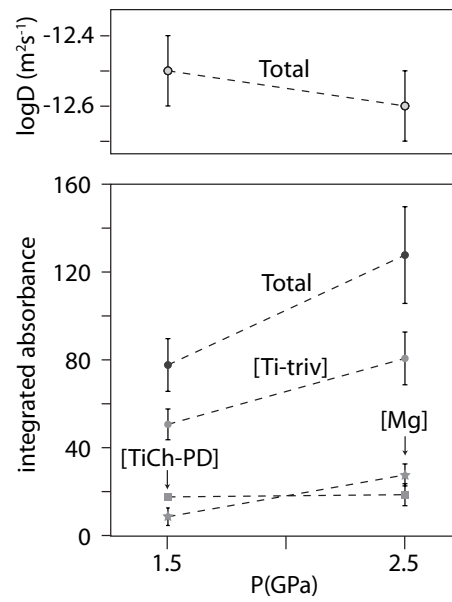


Figure 11

